nature photonics

Supplementary information

https://doi.org/10.1038/s41566-024-01577-x

Intrinsic optical bistability of photon avalanching nanocrystals

In the format provided by the authors and unedited

Table of Contents

1. Materials and Methods

1.1 Materials

Lead acetate trihydrate ($Pb(CH_3COO)_2 \cdot 3H_2O$, 99.99%) was purchased from Alfa Aesar, Potassium carbonate, anhydrous (K_2CO_3, 99%), Neodymium (III) acetate hydrate ($Nd(CH_3COO)_3 \cdot xH_2O$, 99.9%), Neodymium (III) chloride ($NdCl_3$, 99.9+%), Yttrium (III) chloride (YCl_3, 99.9+%), myristoyl chloride (97%), ammonium fluoride (NH_4F, 99.9%), oleic acid (OA, 90%), octadecene (ODE, technical grade, 90%), and hexane (anhydrous, 99.5%) were purchased from Sigma-Aldrich. Sodium oleate (>97%) was purchased from TCI. All chemicals were used without any further purification.

1.2 Synthesis of $KPb_2Cl_5:Nd^{3+}$ nanocrystals

$KPb_2Cl_5:Nd^{3+}$ nanocrystals were synthesized according to the procedure by Zhang et al.[1] In a typical synthesis, K_2CO_3 (6.9 mg), $Pb(CH_3COO)_2 \cdot 3H_2O$ (76 mg), 3 mL of OA, 0.5 mL of OM, $Nd(CH_3COO)_3 \cdot xH_2O$ (0.25 mmol), and 6 mL of ODE were added into a 50 mL 3-neck round bottom flask. The solution was stirred and degassed on a Schlenk line at 40 °C for 5 min and then heated to 120 °C degassing for 1 hour. Subsequently, the temperature was increased to 260 °C under N_2. Upon reaching this temperature, 0.3 mL of myristoyl chloride precursor was swiftly injected. The reaction flask was immediately immersed in an ice−water bath. Finally, after adding 5 mL of hexane, the crude solution was centrifuged at 3000 rpm for 5 min. The supernatant was discarded, and the precipitate was redispersed in 5 mL of hexane for further use. Nd^{3+}-doped KPb_2Cl_5 NPs with varying Nd^{3+} concentrations were synthesized following the method described above, except the nominal Nd^{3+} amount was varied using values of 0.004, 0.01, 0.04 and 0.10 mmol $Nd(CH_3COO)_3 \cdot xH_2O$.

1.3 Synthesis of $NaYF_4:Nd^{3+}$ nanocrystals

$NaYF_4:Nd^{3+}$ nanoparticles were synthesized using a previously described synthesis[2], with some modification. To a dry 100 mL 3-neck round bottom flask (0.9 mmol, 175.7 mg) of YCl_3 and (0.1 mmol, 25.1 mg) of $NdCl_3$ were added together with OA (6 mL) and ODE (14 mL). The flask was stirred, placed under vacuum, and heated to 100 ºC for 1 hour, causing the solution to become clear. The flask was then filled with N_2, and sodium oleate (2.5 mmol, 761.1 mg) and NH_4F (4 mmol, 148.1 mg) were added. The flask was subsequently placed under vacuum and stirred for another 20 min, followed by N_2 flushing 3 times. The reaction was heated to 320 ºC and allowed to react under N_2. After 40 min of reaction time, the flask was rapidly cooled down to room temperature by a strong stream of air, and nanoparticles were isolated with the help of EtOH (20 mL) and centrifugation (3000 x g, 5 min). The nanoparticles were washed twice with hexane:EtOH (1:1 *v*/*v*) and redispersed in 4 mL of hexane for storage.

1.4 Structural characterization

Transmission electron microscopy (TEM) and high-angle annular dark-field scanning TEM (HAADF-STEM) images of $KPb_2Cl_5:Nd^{3+}$ nanocrystals were acquired using a FEI ThemIS 60−300 STEM/TEM (ThermoFisher Scientific, US) operated at 300 kV at the LBNL National Center for Electron Microscopy. Energy Dispersive

Spectroscopy (EDS) mapping was performed using a Bruker Super-X Quad windowless detector with a solid angle of 0.7 sr. TEM samples were prepared by drop-casting nanoparticles dispersed in hexane onto a copper TEM grid with an ultra-thin graphene layer (Ted Pella). The TEM imaging of $KPb_2Cl_5:Nd^{3+}$ and $NaYF_4:Nd^{3+}$ nanocrystals was also performed with a transmission electron microscope (JEOL 2100F) operated at an accelerating voltage of 200 kV. The Nd to Pb atomic fraction on the EDS map was calculated by removing the background signal contribution and integrating the Nd and Pb X-ray signals for each nanocrystal region. To avoid potential X-ray signal overlap, only Nd-L and Pb-L were used to calculate the atomic fractions of Nd and Pb. The molar percentage of Nd^{3+} dopants in KPb_2Cl_5 nanocrystals was measured by elemental analysis using inductively coupled plasma optical emission spectroscopy (Varian ICP-OES 720 Series)[1].

1.5 Optical characterization

Photon avalanche emission of $KPb_2Cl_5:Nd^{3+}$ nanocrystals was measured in NP films prepared by drop-casting chloroform dispersions with NPs onto glass coverslips (0.13 mm thickness) or silicon substrates. Films were characterized using a custom-built confocal inverted microscope (see principal scheme below) equipped with Lake Shore Janis ST-500 cryostat. The sample was excited by a 1064 nm continuous-wave laser source (Opus 1064 3000, Laser Quantum) coupled through a 950 nm short-pass dichroic mirror and a long working distance air objective (60x 0.7NA, Nikon). Emission spectra were collected by the same objective, spectrally filtered using a 950 short-pass filter, and imaged onto an EMCCD camera (Andor iXon Ultra 897) equipped spectrometer (Acton Research Corp., SpectraPro-300i). Absolute intensities of Nd^{3+} emission lines at 810 nm or 880 nm were measured using an avalanche photodiode and 809/81 nm or 935/170 nm band-pass filters, respectively. For power dependence measurements, a continuously variable, reflective neutral density filter wheel (Thorlabs) was inserted in the laser beam path for coarse power selection, and fine power steps were obtained by motorized rotation of a half-wave plate coupled with a Glan-Taylor prism (Thorlabs), power selection was synchronized and automated with the collection system. Powers were simultaneously recorded by a Thorlabs power meter from a glass coverslip to reflect ~10% of the incoming flux. Average excitation power densities were calculated using measured laser powers and the $1/e^2$ area for the employed excitation wavelength and microscope objective. Photoswitching experiments were done by co-aligning Ti:Sapphire laser (Chameleon Ultra II, Coherent) onto the sample. All power-dependent data is presented and analyzed without post-acquisition treatment (e.g., background subtraction).

Temporally-resolved luminescence data was collected with APD coupled to a time-correlated single photon counter (TCSPC, HydraHarp 400), which was used to tag photon arrival times of luminescence signal with respect to the laser shutoff trigger event. An optical chopper was used to vary the excitation frequency from 20 to 1000 Hz (variable duty cycle blade: MC1F10A, Thorlabs) and from 120 to 6000 Hz (50% duty cycle blade: MC1F60, Thorlabs).

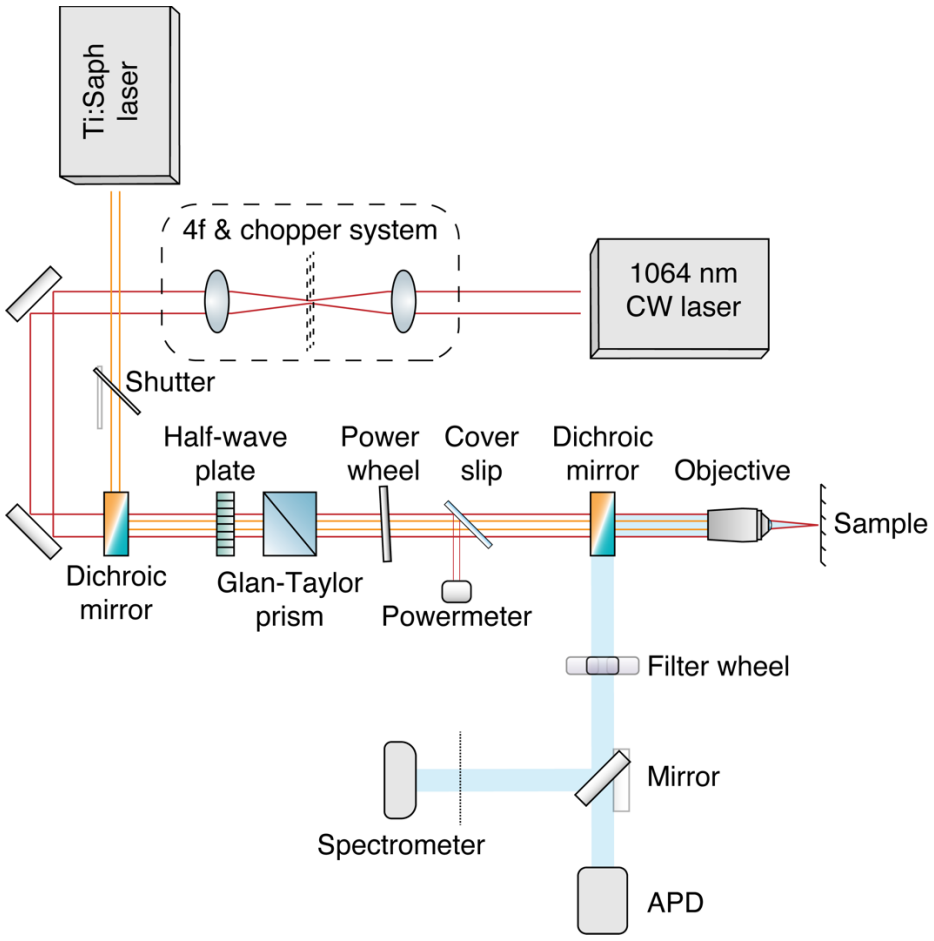

Principle arrangement of the custom-built confocal laser scanning microscope, equipped with 1064 nm CW laser, tunable-wavelength Ti:Saph laser, automatized coarse and fine power adjustment by power wheel and (half-wave plate + Glan-Taylor prism), respectively, and spectrometer or APD baser photoluminescence detection.

1.6 Analysis of luminescence hysteresis

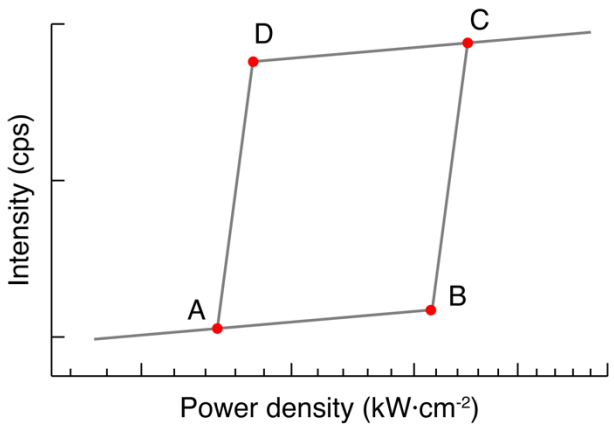

A schematic representation of an intensity (I) vs power density (P) graph, with key transition points of the hysteresis curve indicated by alphabetical indices A, B, C, and D.

To analyze photoluminescence hysteresis of $KPb_2Cl_5:Nd^{3+}$ nanocrystals, we have estimated the switch-on threshold, hysteresis width, and switch-on contrast from the power-dependent photoluminescence plots (schematically represented as *I* vs *P* in the above figure) as follows:

$$Switch-on\ theshold = P_B \tag{S1}$$

$$Hysteresis\ width = \frac{P_C - P_B}{2} - \frac{P_A - P_D}{2} \tag{S2}$$

$$Switch-on\ contrast = 10 * log_{10}\left[\frac{(I_C - I_B)}{I_{noise}}\right] \tag{S3}$$

Here, I_{noise} = 82 cps, the average background noise intensity attainable with our setup.

2. Structural characterization of $KPb_2Cl_5:Nd^{3+}$ ANPs

To characterize $KPb_2Cl_5:Nd^{3+}$ ANPs, we performed a detailed TEM/STEM study on the as-synthesized samples from two different batches (Supplementary Figure S1). The as-synthesized $KPb_2Cl_5:Nd^{3+}$ ANPs exhibit prolate morphology with an average length of 61±13 nm and 63±10 nm, measured for the two batches of nanocrystals. The larger size and lower surface-area-to-volume ratio of these nanocrystals minimize the non-radiative quenching of Nd^{3+} dopants by surface vibrations. We further performed STEM-EDS analysis on two isolated $KPb_2Cl_5:Nd^{3+}$ ANPs (Supplementary Figure S2) and observed a homogeneous distribution of elements. From the corresponding EDS spectra, we calculate the Nd^{3+} doping concentration ([Nd^{3+}] per Pb site) to be 12 ± 2 % and 17 ± 3 % in the two ANPs, which is in good agreement with the average [Nd^{3+}] analyzed via ICP-OES.

We note that KPb_2Cl_5 crystals have two crystallographically distinct Pb^{2+} sites with coordination numbers (CN) = 7 for Pb(1) and 9 for Pb(2) [3,4]. Since Ln^{3+} incorporation is favored in sites with greater CN [5], Ln^{3+} ions preferentially substitute Pb(2) [3]. Subsequently, when Ln^{3+} ions enter the KPb_2Cl_5 matrix, a K^+ vacancy is formed to compensate for the charge imbalance[3,6].

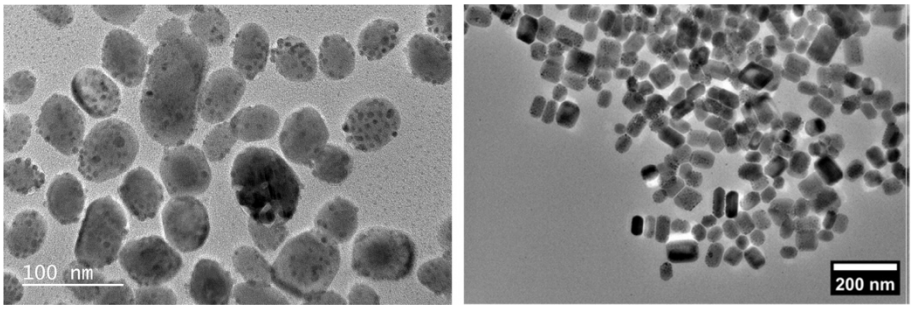

Supplementary Figure S1. Representative TEM images of the bistable $KPb_2Cl_5:Nd^{3+}$ photon avalanching nanoparticles (ANPs) from two different synthesis batches. We note that exposure to e-beam induces degradation of the nanocrystals, seen as the appearance of the darker contrast $PbCl_2$ spots, consistent with other reports[7–9]. Importantly, these $PbCl_2$ accumulations result from nanocrystals being mildly sensitive to the environment (e.g., moisture or e-beam) during long-term storage but do not impact the performance of as-synthesized or nondegraded $KPb_2Cl_5:Nd^{3+}$ ANPs.

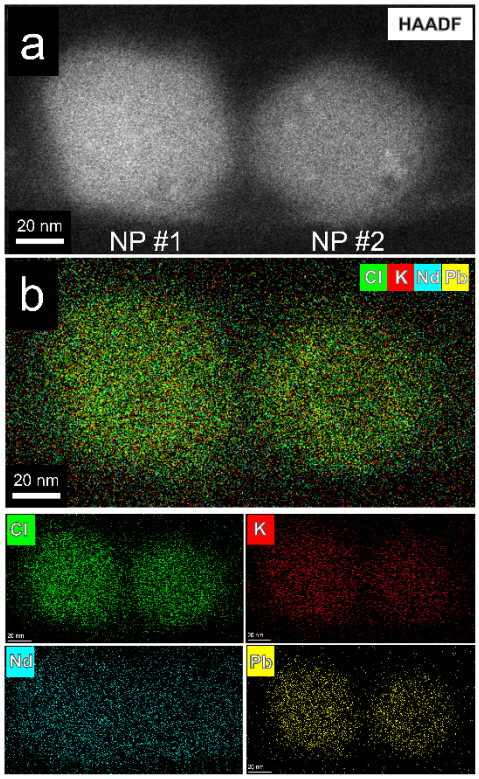

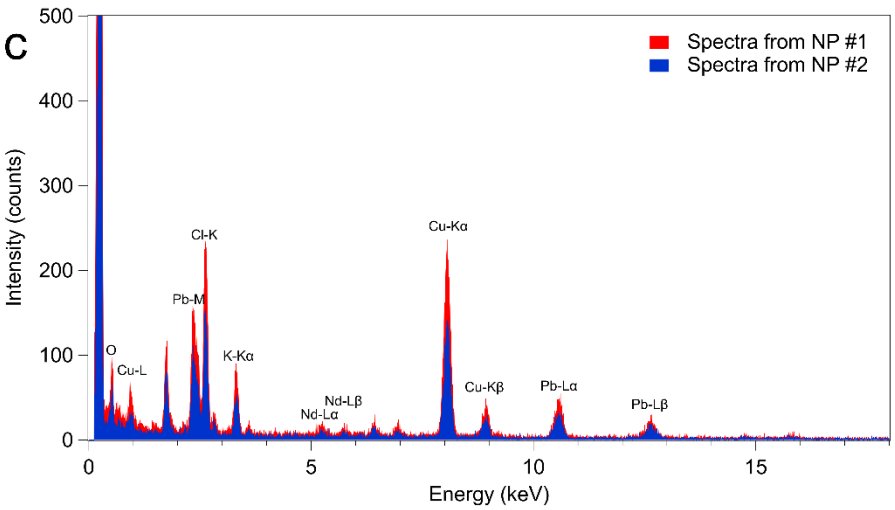

Nanoparticle	Nd Atomic Fraction (%)	Pb Atomic Fraction (%)
#1	12 ± 2	88 ± 14
#2	17± 3	83 ± 13

Supplementary Figure S2. **A** – HAADF-STEM image of two KPb_2Cl_5:Nd^{3+} nanocrystals analyzed via STEM-EDS for elemental composition. Analyzed KPb_2Cl_5:Nd^{3+} nanocrystals are referred to as NP #1 (left nanocrystal) and NP #2 (right nanocrystal). **B** – Corresponding STEM-EDS elemental mapping of merged and individual Cl-K, K-K, Nd-L, and Pb-L channels. **C** – EDS spectra of the two analyzed nanocrystals, with the calculated Nd to Pb atomic fractions of 12% and 17% in NP #1 and NP #2, respectively. This result is in good agreement with the average [Nd^{3+}], analyzed via ICP-OES[1].

3. MPR rate vs host phonon energy and temperature

The scaling of MPR rate (W) was determined using[10]:

$$W = W_0 e^{-(\beta \Delta E)} \left(1 - exp\left[\frac{\hbar\omega}{k_B T}\right]\right)^{-p} \quad \text{(S4)}$$

where W_0 and β are host-dependent parameters, ΔE energy gap between adjacent states, $\hbar\omega$ host phonon energy, k_B Boltzmann constant, T temperature, and p number of phonons involved in bridging the energy gap:

$$p = \frac{\Delta E}{\hbar\omega} \quad \text{(S5)}$$

Supplementary Table S1. Host-dependent phonon relaxation parameters and energy gap values between first excited and ground states of Nd^{3+} ions in $NaYF_4$ and KPb_2Cl_5 hosts.

Parameter [units]	KPb_2Cl_5	$NaYF_4$
Phonon cutoff energy $\hbar\omega$ [cm^{-1}]	250 ref:1,6	450 ref:11
W_0 rate constant [s^{-1}]	$0.5 \cdot 10^7$	$1.0 \cdot 10^7$
β MPR rate constant [cm]	$9.2 \cdot 10^{-3}$	$2.0 \cdot 10^{-3}$
ΔE energy gap ($^4I_{11/2}$–$^4I_{9/2}$) [cm^{-1}]	1900	1828

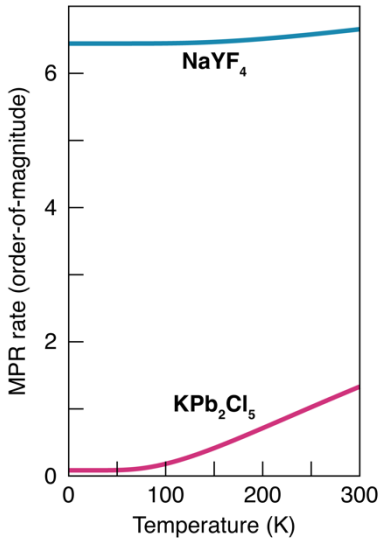

Supplementary Figure S3. Calculated temperature-dependent scaling of multiphonon relaxation (MPR) rates between the first excited and ground state ($^4I_{11/2} \rightarrow {}^4I_{9/2}$) of Nd^{3+} ions in $NaYF_4$ and KPb_2Cl_5 hosts.

4. Robustness of IOB to measurement conditions

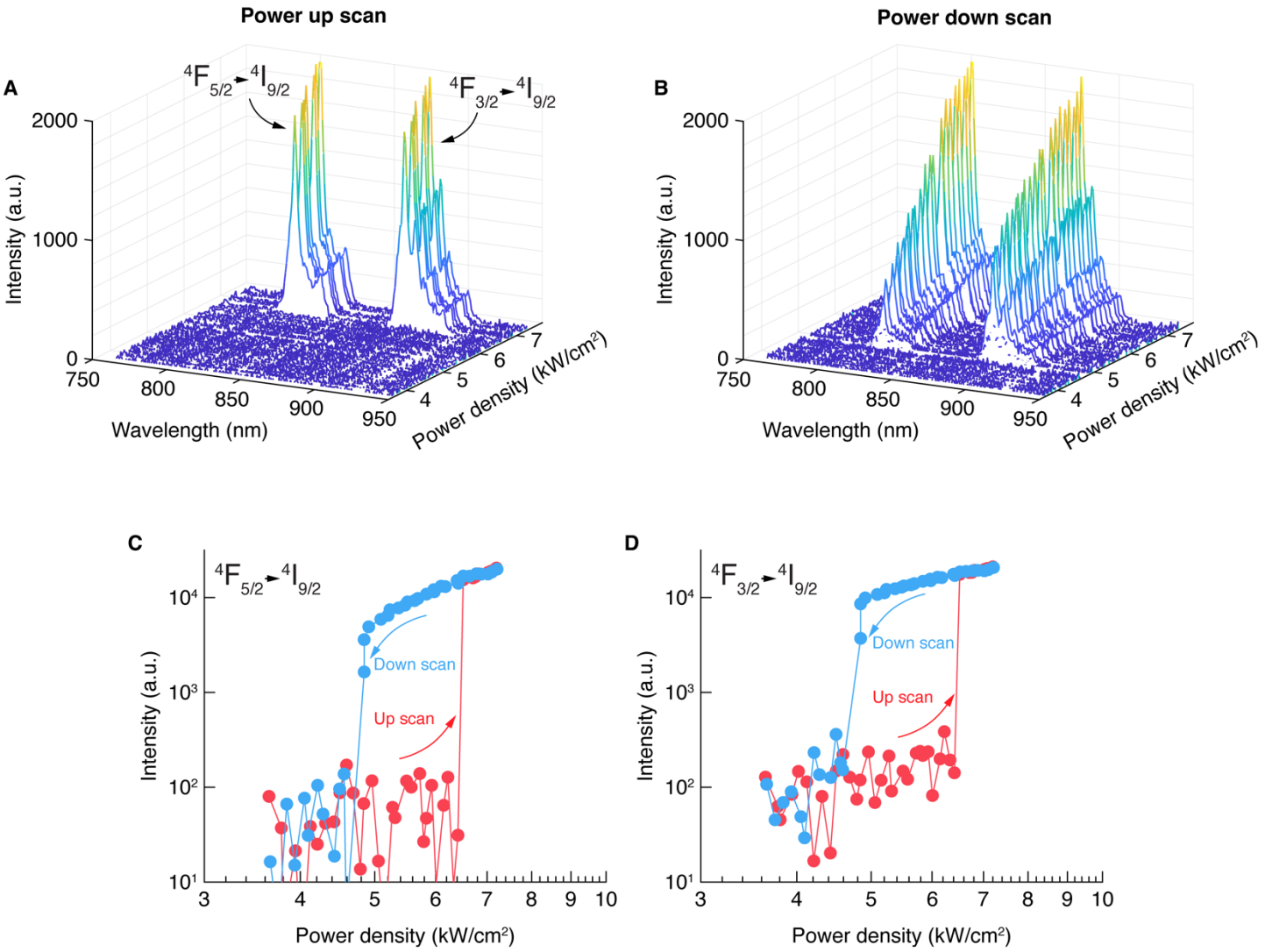

Supplementary Figure S4. A, B – Pump (1064 nm) power dependence of Nd^{3+} emission in $KPb_2Cl_5:Nd^{3+}$ ANPs at 77 K registered with a spectrometer, instead of an APD as in all other power-dependent measurements. Spectra of ANPs can be observed at lower pump powers in the down scan (**B**) compared to the up scan (**A**). **C, D** – Integrated Nd^{3+} emission intensity in $KPb_2Cl_5:Nd^{3+}$ ANPs at 77 K against pump power, corresponding to $^4F_{5/2} \rightarrow {}^4I_{9/2}$ (integration range 800-830 nm, **C**) and $^4F_{3/2} \rightarrow {}^4I_{9/2}$ (integration range 870-900 nm, **D**) radiative transitions. Red data points represent scanning with increasing powers (up scan) and blue with decreasing (down scan).

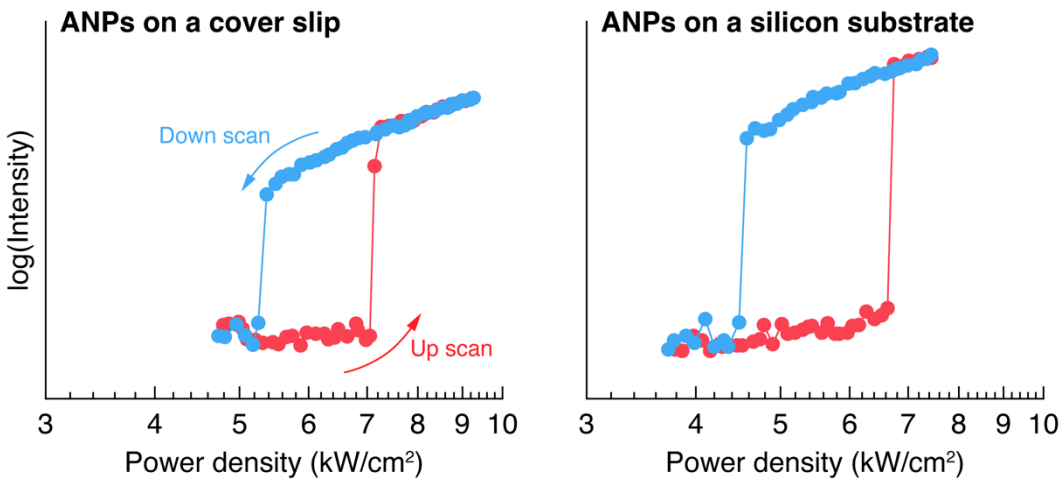

Supplementary Figure S5. Pump (1064 nm) power dependence of Nd^{3+} emission (810 nm, $^4F_{5/2} \rightarrow {}^4I_{9/2}$) in $KPb_2Cl_5:Nd^{3+}$ ANPs at 77 K. ANPs were deposited either on a coverslip (left) or on a silicon substrate (right). Red data points represent scanning with increasing powers (up scan) and blue with decreasing (down scan).

5. Measuring IOB in $KPb_2Cl_5:Nd^{3+}$ ANPs using different photodiode dwell times

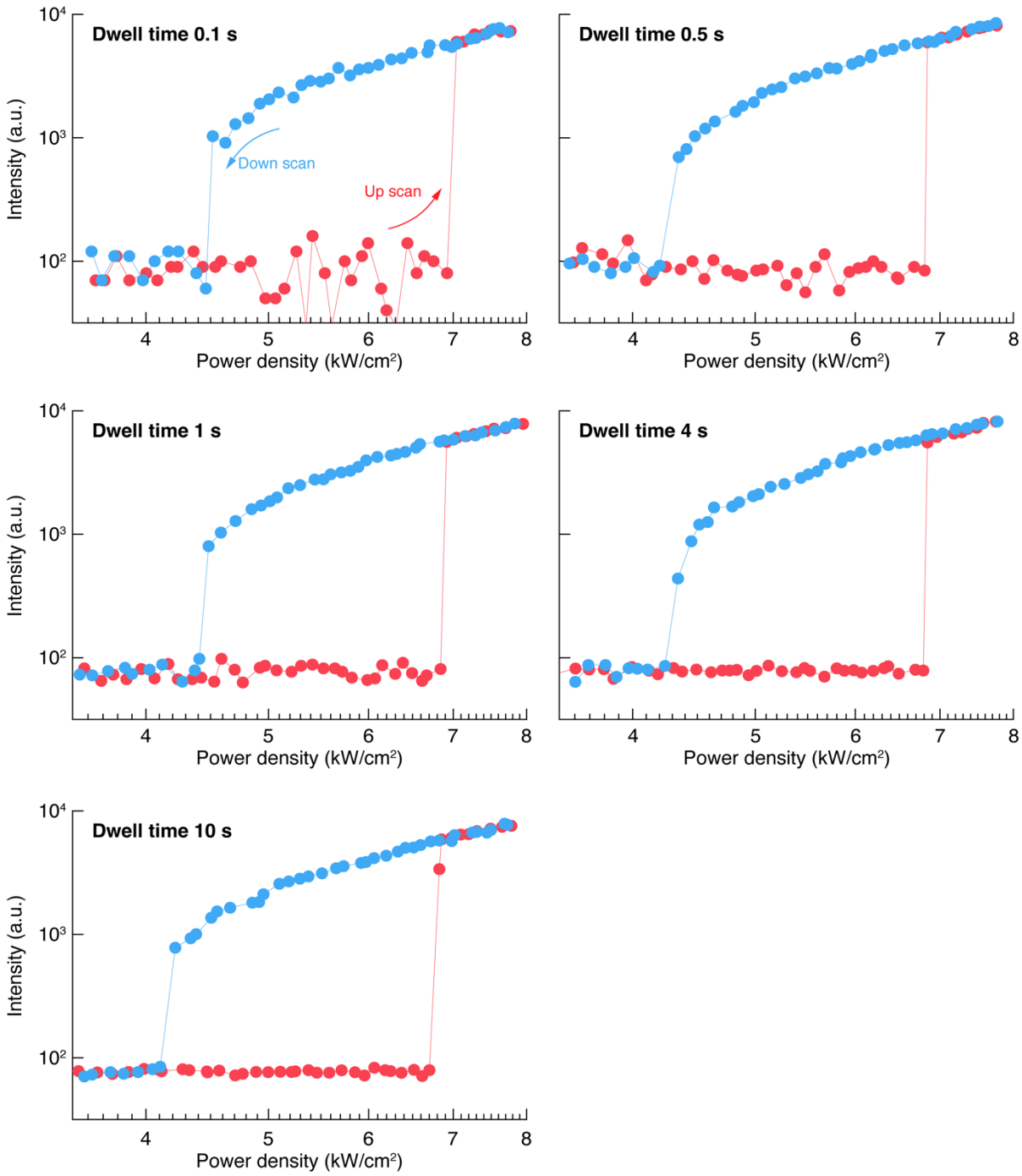

Supplementary Figure S6. Pump (1064 nm) power dependence of Nd^{3+} emission (810 nm, $^4F_{5/2} \rightarrow {}^4I_{9/2}$) in $KPb_2Cl_5:Nd^{3+}$ ANPs at 77 K, using different signal dwell time per set power value. Red data points represent scanning with increasing powers (up scan) and blue with decreasing (down scan). Here, dwell time corresponds to the time taken by the APD to measure luminescence intensity in counts-per-second (cps) at a given excitation power density. Longer dwell times are equivalent to signal averaging and reduce uncertainty in the determined luminescence intensity. A signal collection delay of 0.5 s was implemented to ensure ANPs reached a steady state before each photoluminescence measurement.

6. IOB in $KPb_2Cl_5:Nd^{3+}$ ANPs: reproducibility and repeatability

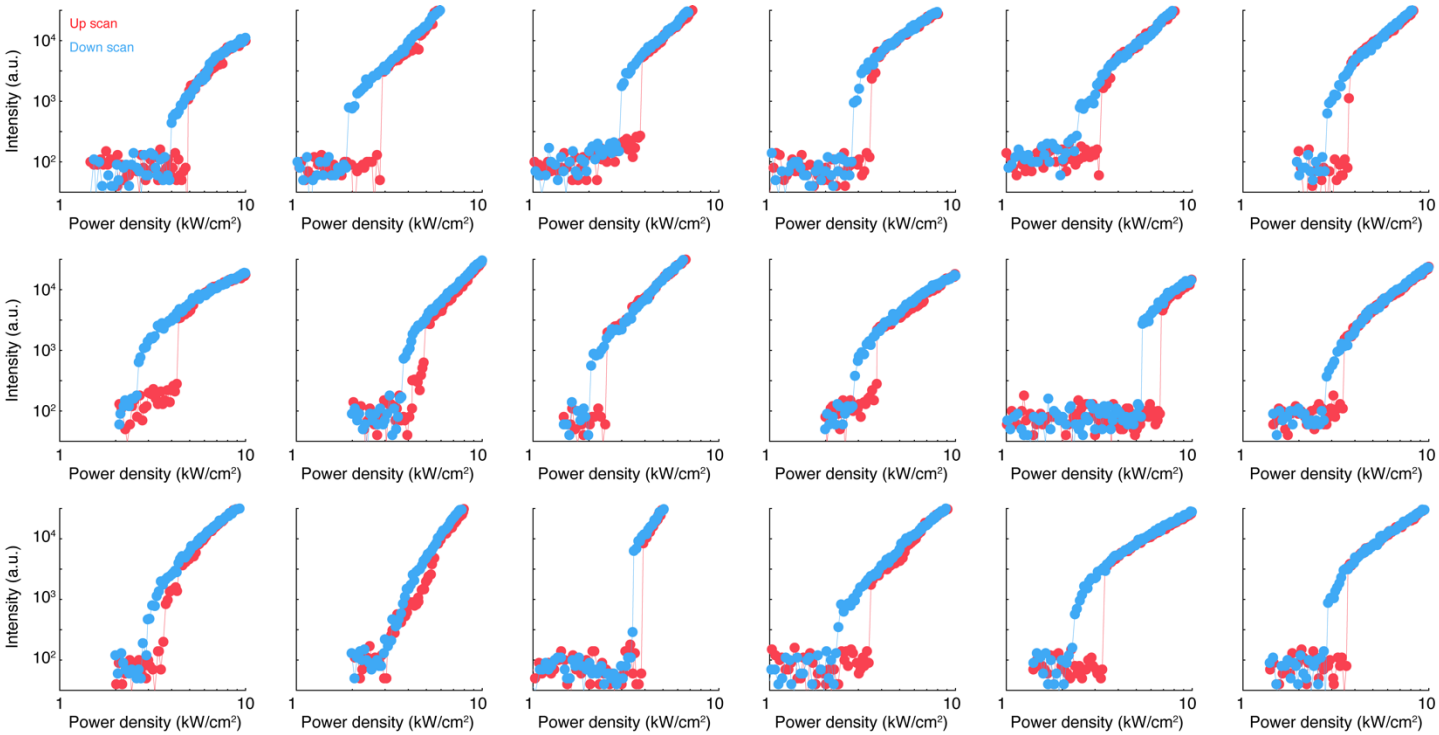

Supplementary Figure S7. Representative pump (1064 nm) power dependence curves of Nd^{3+} emission (810 nm, $^4F_{5/2} \rightarrow {}^4I_{9/2}$) in $KPb_2Cl_5:Nd^{3+}$ ANPs at 77 K. Data were taken for multiple spots of the film sample. Red data points represent scanning with increasing powers (up scan) and blue with decreasing (down scan).

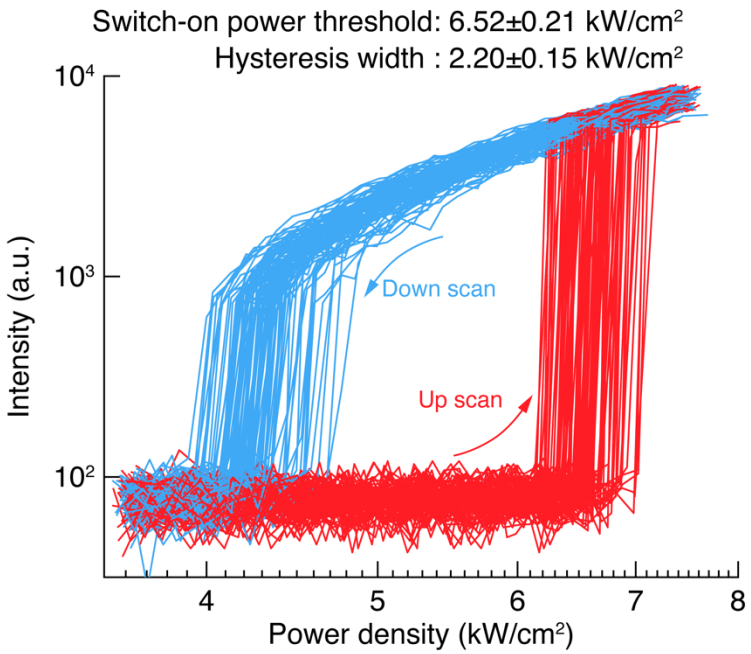

Supplementary Figure S8. Pump (1064 nm) power dependence of Nd^{3+} emission (810 nm, $^4F_{5/2} \rightarrow {}^4I_{9/2}$) in KPb_2Cl_5: Nd^{3+} ANPs at 77 K measured consecutively across 100 cycles over 12 hours. Red lines represent scanning with increasing powers (up scan) and blue with decreasing powers (down scan). Average ± standard deviation values of the switch-on threshold and hysteresis width are shown above the graph.

7. Supplementary Table S2. Comparison of different materials and systems that show optical bistability. Switch-on contrast and threshold values are best estimates for works that do not provide them explicitly. [a] Average observed contrast. Contrast calculated as the intensity difference between bright and dark states divided by the noise intensity. For literature values, we report maximum contrast represented. [b] Contrast as calculated by the authors. [c] Data to assess the size is not provided. [d] The origin of bistability is either uncertain or fits better the explanation given by ref. 12. [e] Qualitative estimate since intensity values are not provided.

Material/system	Scale (size)	Excitation wavelength	Observable	Temperature	Switching contrast	Switching threshold	Origin of bistability	Ref.
Silver-coated CdS	Nano (15 nm)	514.5 nm	Scatter/transmission	RT	1.4	52 kW/cm^2 (~650 mW)	Non-thermal	13
Amorphous silicon Mie resonator	Nano (155 x 142 nm)	785 nm	Scatter/transmission	RT	10	360 kW/cm^2	Thermal	14
Silicon nanowire-gold nanorod hybrid	Nano (15 nm x 16 µm)	1310 nm	Scatter/transmission	RT	14	11.7 µW	Non-thermal	15
$KPb_2Cl_5:Nd^{3+}$	Nano (61 nm)	1064 nm	Photoluminescence	77-150 K	218 (max.) 43 (mean)[a]	5.2 kW/cm^2 (64 µW)	Non-thermal	This work
Yb^{3+}, Er^{3+}-co-doped phosphate glass	Micro (50 µm)	1550 nm	Photoluminescence	RT	21[b]	8.5 mW	Thermal	16
InP/InGaAsP photonic crystal	Micro (4 x 0.3 x 0.15 µm)	1550 nm	Scatter/transmission	RT	100	25 nW	Non-thermal	17
$ZrO_2:Yb^{3+},Tm^{3+}$	Bulk nanocrystalline[c]	973 nm	Photoluminescence	RT	2	>200 mW	Thermal	18
$LiNdP_4O_{12}$	Bulk nanocrystalline[c]	808 nm	Photoluminescence	RT	3.2	>100 mW	Tentatively thermal[d]	19
$Cs_3Yb_2Br_9$	Bulk	944 nm	Photoluminescence	5-15 K	High vs noise[e]	2.27 kW/cm^2	Tentatively thermal[d]	20
$NdPO_4:Yb^{3+}$	Bulk	808 nm	Photoluminescence	15-200 K	Low vs noise[e]	0.5 kW/cm^2	Thermal	21
$CsCdBr_3:Yb^{3+}$, Er^{3+}	Bulk	943 nm	Photoluminescence	6-25 K	High vs noise[e]	4 kW/cm^2	Thermal	22
$CsCdBr_3:Yb^{3+}$	Bulk	944 nm	Photoluminescence	14-35 K	High vs noise[e]	4 kW/cm^2	Tentatively thermal[d]	23
Y_2O_3	Bulk	980 nm	Photoinduced blackbody radiation	RT	25	22 W	Non-thermal	24
Yb^{3+}, Tm^{3+}-co-doped glass	Bulk	960 nm	Photoluminescence	RT	High vs noise[e]	370 mW	Tentatively thermal[d]	25
$Y_2WO_6:Yb^{3+},Tm^{3+}$	Bulk	980 nm	Photoluminescence	RT	1.5	453 mW	Tentatively thermal[d]	26
Er^{3+}-doped fiber	Bulk	980 nm	Photoluminescence	RT	2500	72 mW	-	27
Yb^{3+}-doped high silica glass	Bulk	980 nm	Photoluminescence	RT	1.3	>2.5 W	Tentatively thermal[d]	28
InSb cavity	Bulk	5497 nm	Scatter/transmission	77 K	1.2	26 mW	Non-thermal	29

8. IOB in KPb_2Cl_5:Nd^{3+} ANPs against Nd^{3+} doping concentration

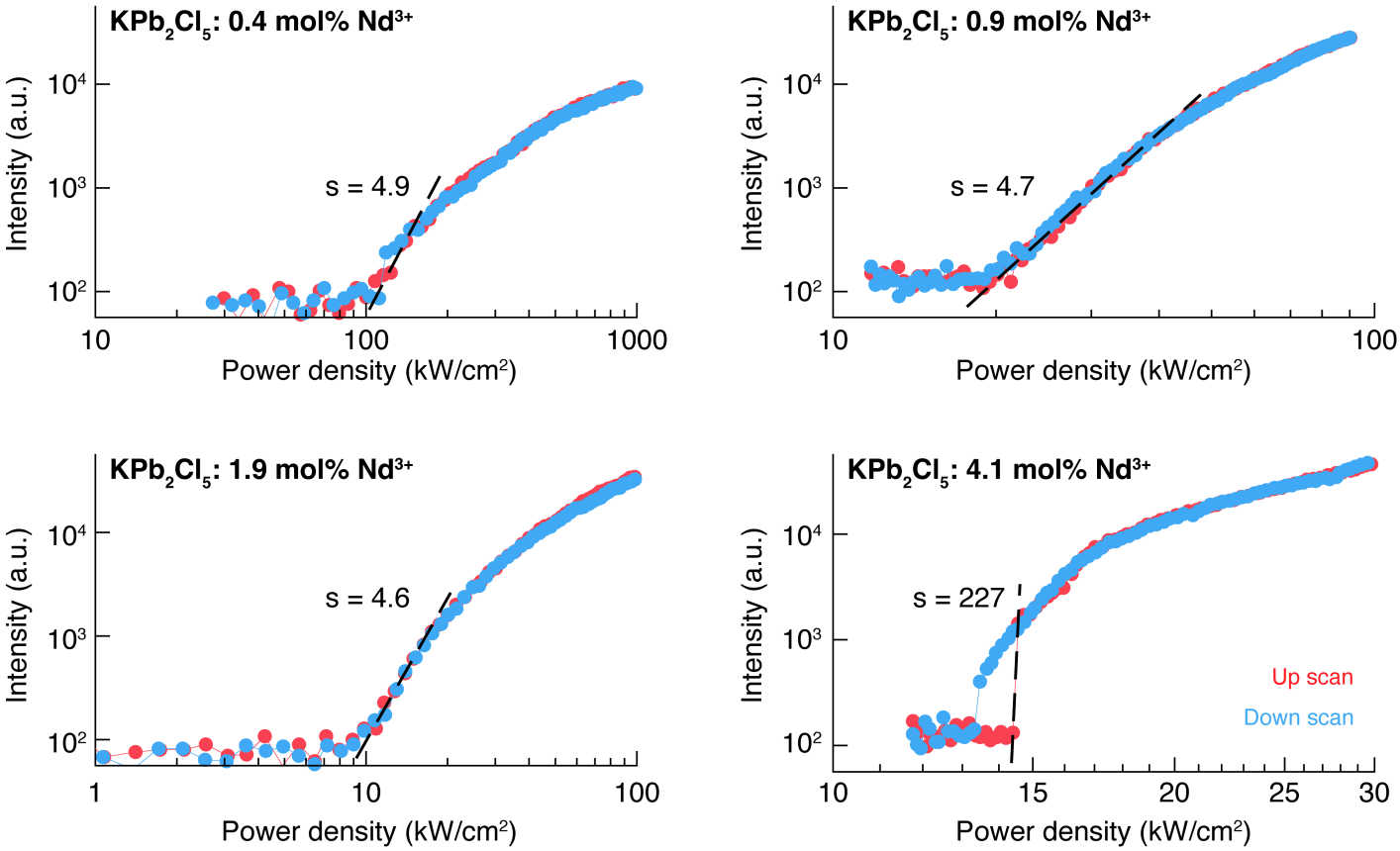

Supplementary Figure S9. Representative pump (1064 nm) power dependence of Nd^{3+} emission (810 nm, $^4F_{5/2} \rightarrow {}^4I_{9/2}$) in KPb_2Cl_5: x mol% Nd^{3+} ANPs at 77 K. Red data points represent scanning with increasing powers (up scan) and blue with decreasing (down scan).

9. Power dependence of $NaYF_4:Nd^{3+}$ nanocrystals at cryogenic temperatures

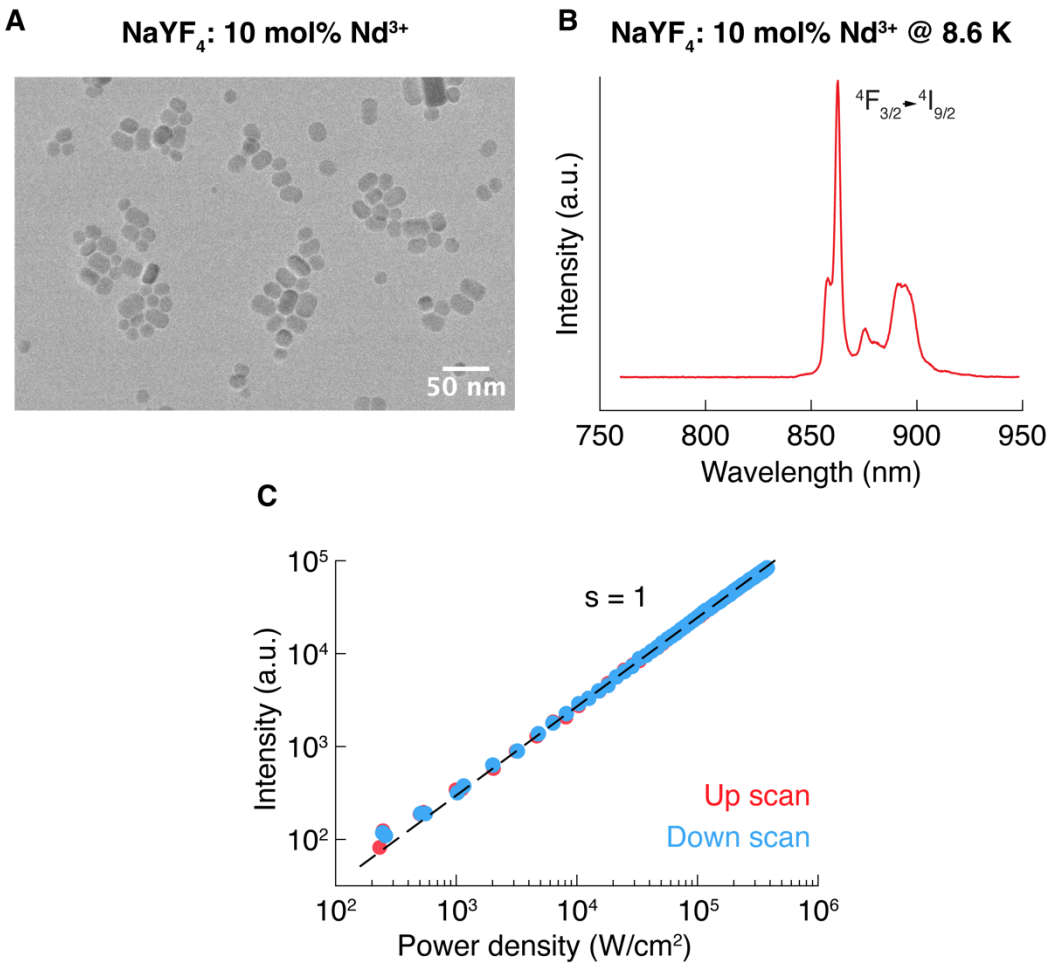

Supplementary Figure S10. A – Representative TEM image $NaYF_4$: 10 mol% Nd^{3+} NPs. **B** – Emission spectrum of $NaYF_4$: 10 mol% Nd^{3+} NPs at 8.6 K under 1064 nm excitation. **C** – Pump (1064 nm) power dependence of Nd^{3+} emission (880 nm, $^4F_{3/2} \rightarrow {}^4I_{9/2}$) in $NaYF_4:Nd^{3+}$ NPs at 8.6 K. Red data points represent scanning with increasing powers (up scan) and blue with decreasing (down scan).

10. Supplementary Note S1. Rate constants and rate equation model

Theoretical description of the system. Since the intensity of a given radiative transition is proportional to the product of the population of the emitting state and the microscopic rate constant for the transition, we used a set of coupled differential equations to describe the instantaneous populations of the Ln^{3+} manifolds[30]. In this population balance model, the population N_i (in nm^{-3}) of a lanthanide $4f^N$ manifold i over time is determined by the incoming and outgoing rates of electric dipole (ED) and magnetic dipole (MD) radiative transitions, nonradiative multiphonon relaxation (MPR) and energy transfer (ET):

$$\frac{dN_i}{dt} = \sum_j \left(N_j A_{ji}^{ED} - N_i A_{ij}^{ED}\right) + \sum_j \left(N_j A_{ji}^{MD} - N_i A_{ij}^{MD}\right) + \left(N_{i+1} W_{i+1,i}^{NR} - N_i W_{i,i-1}^{NR}\right) + \sum_{ij,kl} \left(N_j N_l P_{ji,kl}^{ET} - N_i N_k P_{ij,lk}^{ET}\right) \quad \text{(S6)}$$

A_{ij}^{ED} and A_{ij}^{MD} (s^{-1}) are the Einstein coefficients for ED and MD radiative transitions from manifold i to j. $W_{i,i-1}^{NR}$(s^{-1}) is the nonradiative MPR rate from the manifold i to the manifold immediately below i. $P_{ij,kl}^{ET}$ ($nm^3 \cdot s^{-1}$) is the microscopic energy transfer parameter for the transfer of energy for the donor i to j transition and the acceptor k to l transition.

Transition probabilities for individual lanthanide ions are calculated using the same theoretical framework as the comprehensive rate equation models described in our previous work[30,31] (see Ref. 32 for the most detailed description). The transitions in trivalent lanthanide ions are $4f^N$ manifold-to-manifold transitions, including single-ion transitions (non-radiative multi-phonon relaxation, electric dipole absorption/emission, and magnetic dipole absorption/emission) and two-ion interactions (dipole-dipole energy transfer). The individual theories and equations behind these transition probabilities are discussed below. Representative rate constants comparing KPb_2Cl_5:Nd^{3+} and $NaYF_4$:Nd^{3+} are given in Supplementary Table S3.

Multiphonon relaxation (MPR) transition probabilities, W_i^{MPR}, from an initial lanthanide manifold i to the level below i are calculated using Van Dijk's modified Energy Gap Law[33]:

$$W_i^{NR} = W_0^{MPR} e^{-\alpha(\Delta E - 2\hbar\omega)} \quad \text{(S7)}$$

where ΔE is the energy gap to the lower manifold and $\hbar\omega$ is the energy of the cutoff phonon energy of the host matrix. $W_0^{MPR}$and α are MPR constants that are consistent across transitions in a given host matrix. W_0^{MPR} is the MPR rate when $\Delta E = 2\hbar\omega_{max}$,

Electric dipole (ED) radiation and absorption probabilities are calculated using Judd-Ofelt (JO) theory[32,34]. The transition probability (in s^{-1}) for electric dipole radiative relaxation, A_{ij}^{ED}, is determined using the three JO parameters (Ω_λ) and the doubly reduced matrix elements of the unit tensor operator $U^{(\lambda)}$ of rank λ, where $\lambda =$ 2,4, or 6:

$$A_{ij}^{ED} = \frac{64\pi^4 e^2 \tilde{v}^3}{3h(2J+1)}[\frac{n(n^2+2)^2}{9}]S_{ij}^{ED} \quad \text{(S8)}$$

$$S_{ij}^{ED} = \sum_{\lambda=2,4,6} \Omega_\lambda | < [SL]J_i||U^{(\lambda)}||[SL]J_j > |^2 \quad \text{(S9)}$$

Here, $\tilde{v}$ is the energy of the transition in wavenumbers, h is Planck's constant, e is the elementary charge, n is the index of refraction of the material, J is the total angular momentum of the initial state, and S_{ij}^{ED} is the electric dipole line strength, using the Gaussian unit system. JO parameters used in this work are shown in Supplementary Table S3.

Supplementary Table S3. Judd-Ofelt parameters and reduced matrix elements.

Parameter	Nd^{3+} in KPb_2Cl_5
Ω_2 (10^{-20} cm^2)	11
Ω_4	8.01
Ω_6	6.19
Source, Ω_λ	Isaenko et al.[35]
Source, $\|<i\|U_\lambda\|j>\|^2$	Kaminskii et al.[10]

For ED absorption, $A_{ij} = \psi\sigma_{ij}$, where ψ is the incident photon flux. The ED absorption cross section integrated over the transition, σ_{ij}^{ED}, is calculated from S_{ij}^{ED} using the relation:

$$\sigma_{int}^{ED} = \frac{8\pi^3 e^2 \tilde{v}}{3hcg_i}\frac{(n^2+2)^2}{9n}S_{ij}^{ED} \quad \text{(S10)}$$

Here, σ_{int}^{ED} is the ED absorption cross section integrated over the entire transition. We handled two cases: resonant and non-resonant (phonon-assisted) absorption. For resonant absorption, we assumed that the laser excitation source has a width of 1 nm, and the absorption peak is a Gaussian curve centered at $\tilde{v}$. In this case, σ_{ij}^{ED} is determined from σ_{int}^{ED} using the expression:

$$\sigma_{ij} = \sigma_{int}^{ED} \frac{1}{w\sqrt{2\pi}} e^{-(\upsilon_{ex}-\tilde{\upsilon})^2/(2w^2)} \quad \text{(S11)}$$

where υ_{ex} is the energy (in wavenumbers) of the excitation source. w is the linewidth of the absorption transition, related to the absorption FWHM by the expression: $w = FWHM_{abs}/(2\sqrt{2ln2})$. For $FWHM_{abs}$ see Supplementary Table S5.

For non-resonant absorption, the cross-section was modified to account for phonon assistance, as for MPR:

$$\sigma_{ij,PA} = \sigma_{ij,0}.e^{-\alpha|\upsilon_{ex}-\tilde{\upsilon}|} \quad \text{(S12)}$$

where $\sigma_{ij,0}$ is the value of the resonant $\sigma_{ij,0}$ when $\upsilon_{ex} = \tilde{\upsilon}$.

Magnetic dipole (MD) radiation and absorption probabilities. The MD radiative rate constant A_{ij}^{MD} is calculated with the equations:

$$A_{ij}^{MD} = \frac{64\pi^4 e^2 \tilde{\upsilon}^3}{3h(2J+1)} n^3 S_{ij}^{MD} \quad \text{(S13)}$$

$$S_{ij}^{MD} = \mu_B^2 | < [SL]J_i||L+2S||[SL]J_j > |^2 \quad \text{(S14)}$$

where μ_B is the Bohr magneton. L and S are the angular momentum and spin operators, respectively. Note: these operators must be used on the eigenvectors of the intermediate coupled states of each lanthanide ion since each manifold total angular momentum J is treated as a linear combination of various LS states with the same J. The integrated MD absorption cross-section and oscillator strength are calculated using the expressions below:

$$\sigma_{\text{int}}^{MD} = \frac{\pi e^2}{mc^2} f_{ij}^{MD} \quad \text{(S15)}$$

$$f_{ij}^{MD} = \frac{8\pi^2 mc\tilde{\upsilon}}{3he^2 g_i} n S_{ij}^{MD} \quad \text{(S16)}$$

Here, σ_{int}^{MD} is the MD absorption cross-section integrated over the entire transition. The actual MD absorption probability is calculated from σ_{int}^{ED} in the same manner described for ED absorption above.

Phonon-assisted energy transfer probabilities. The orientation-averaged rate of dipole-dipole energy transfer $W_{ij,kl}^{ET}$ with donor transition $i \rightarrow j$ and acceptor transition $k \rightarrow l$ is described as a function of the inter-ion distance R and the ED line strengths S^{ED} of the donor and acceptor transitions[36]:

$$W_{ij,kl}^{ET} = \frac{C_{DA,ijkl}}{R^6} \tag{S17}$$

$$C_{DA,ijkl} = \frac{8\pi^2 e^4 s_0}{3h^2 c g_i g_k} \left(\frac{n^2+2}{3n}\right)^4 S_{ij}^{ED} S_{kl}^{ED} \tag{S18}$$

In this expression, $C_{DA,ijkl}$ is the energy transfer micro-parameter, g_i is the $2J+1$ number of states in manifold i, and s_0 is the overlap integral between the normalized donor emission spectrum and acceptor absorption spectrum. To account for phonon assistance during non-resonant energy transfer, the phonon-assisted energy transfer micro-parameter is used in place of the resonant ET micro-parameter and is calculated as[37]:

$$C_{DA}^{PAET} = C_{DA,ijkl} \cdot exp[-\beta_{MPR}\Delta E] \tag{S19}$$

where $\beta_{MPR} = \alpha - \ln(2)/\hbar\omega$, and ΔE is the net energy difference between the donor and acceptor transitions. $C_{DA,ijkl}$ is the energy transfer micro-parameter assuming a resonant ET process, calculated using eq. S18.

To account for energy transfer over all possible donor-acceptor distances *R* in a nanocrystal, the total phonon-assisted energy transfer (PAET) rate constant for a given donor can be calculated by integrating Eq. S17 over all *R* (ref: 38). In the case of a homogeneously doped material (see Supporting Information of ref: 32), we can define the PAET microparameter as:

$$W_{ij,kl,avg}^{PAET} = \frac{4\pi}{3} N_A C_{DA}^{PAET} R_{\min}^{-3} = N_A P_{ij,kl}^{MAET} \tag{S20}$$

To make the rate constant independent from the acceptor population, Eq. S6 uses the constant, $P_{ij,kl}^{MAET}$ (units of cm^3), whose relationship with $W_{ij,kl,avg}^{MAET}$ is shown above.

Supplementary Table S4. Non-radiative and radiative rate constants and energy transfer (ET) microparameters for the most prominent Nd^{3+} transitions in $NaYF_4$ and KPb_2Cl_5 hosts. Note that the difference in MPR rate constants between the two host matrices has the greatest impact on the Nd^{3+} photoactivation dynamics. [a] Transitions in parentheses denote complementary cross-relaxation (CR) transitions.

Transition type	Transition $i \rightarrow j$[a]	$KPb_2Cl_5:Nd^{3+}$	$NaYF_4:Nd^{3+}$
		Rate constant (s^{-1})	
MPR	$^4I_{11/2} \rightarrow {}^4I_{9/2}$	**185.85**	**654905.30**
	$^4I_{13/2} \rightarrow {}^4I_{11/2}$	98.39	397131.51
	$^4I_{15/2} \rightarrow {}^4I_{13/2}$	4.92	236160.87
	$^4F_{3/2} \rightarrow {}^4I_{15/2}$	2.78×10^{-16}	2.27
ED abs.	$^4I_{9/2} \rightarrow {}^4F_{3/2}$	0.0023	0.227
	$^4I_{11/2} \rightarrow {}^4F_{3/2}$	125.23	246.09
ED em.	$^4F_{3/2} \rightarrow {}^4I_J$ (J = 9/2, 11/2, 13/2)	4709.96	4502.91
Cross-relaxation (CR)		ET microparameter ($\times 10^{-40}$ cm^6/s)	
CR1	$^4I_{13/2} \rightarrow {}^4I_{11/2}$ ($^4I_{9/2} \rightarrow {}^4I_{11/2}$)	363	1598
CR2	$^4I_{15/2} \rightarrow {}^4I_{13/2}$ ($^4I_{9/2} \rightarrow {}^4I_{11/2}$)	351	1217
CR3	$^4F_{3/2} \rightarrow {}^4I_{15/2}$ ($^4I_{9/2} \rightarrow {}^4I_{15/2}$)	0.291	n/a
CR4	$^4F_{3/2} \rightarrow {}^4I_{13/2}$ ($^4I_{9/2} \rightarrow {}^4I_{15/2}$)	0.564	1.75
CR5	$^4F_{3/2} \rightarrow {}^4I_{15/2}$ ($^4I_{9/2} \rightarrow {}^4I_{13/2}$)	0.812	2.49

Calculation methods. We calculated the steady-state population of each Nd^{3+} manifold under a given irradiation through numerical integration of the rate equations in Equation S6, which account for tens of thousands of simultaneous transitions. When performing power-dependent simulations, the population of Nd^{3+} manifolds under a given power density value was simulated starting from the populations obtained at a prior power value. Cross-relaxation knock-out experiments were performed by ignoring transitions that met specified $i \rightarrow j$ & $l \rightarrow k$ criteria during the assembly of rate equations (Supplementary Figure S11)[31].

Kinetic calculations were performed according to the method of Chan et al. using Igor Pro 7 (Wavemetrics). N ordinary differential equations, which represent the population of each N manifold in the simulated system, were solved numerically using the Igor Pro Backwards Differentiation Formula integration method. Calculation parameters are given in Supplementary Tables S3 and S5.

Supplementary Table S5. General simulation parameters. [a] Simulation time period of 2000 ms ensures that the simulated system reaches a steady state for any excitation laser power density.

Parameter	Value	Units
Simulation time period[a]	2000	ms
Radiative rate (A_{ij}) threshold	10^{-4}	s^{-1}
Phonon energy[1,6]	250	cm^{-1}
W^0_{MPR} rate constant[33]	$0.5 \cdot 10^{7}$	s^{-1}
α MPR rate constant[33]	$12 \cdot 10^{-3}$	cm
Index of refraction	1.96	-
Volume per potential dopant site	0.1082	nm^3
Minimum dopant distance	0.4765	nm
Absorption FWHM	1000	cm^{-1}
Incident laser power density	10^3-10^4	W/cm^2
Incident excitation wavelength	1064	nm

11. Mechanistic investigation of IOB

11.1 Additional knockout simulation data

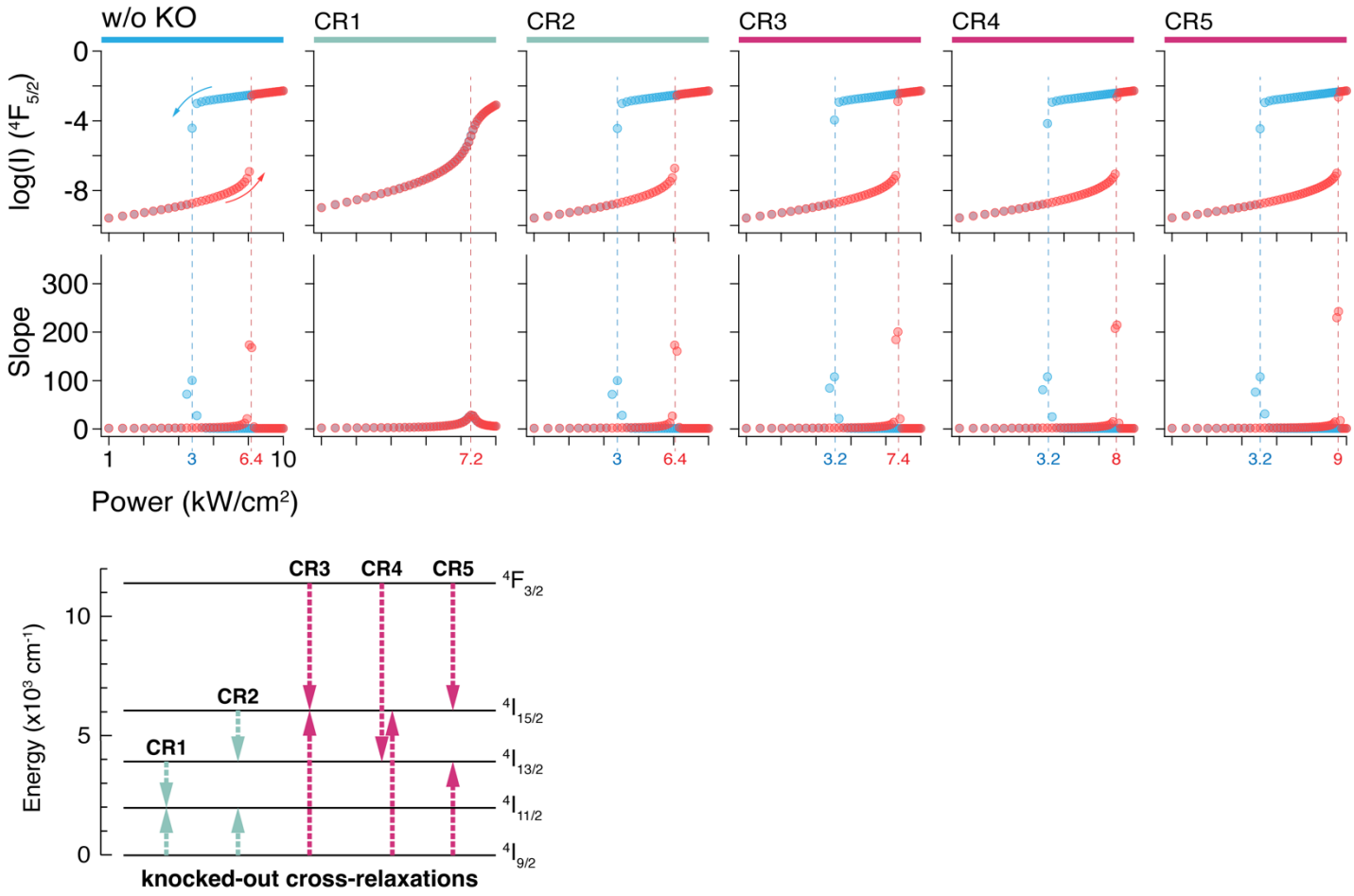

Supplementary Figure S11. Simulated pump (1064 nm) power dependence of Nd^{3+} emission (810 nm, $^4F_{5/2} \rightarrow {}^4I_{9/2}$) in KPb_2Cl_5: 20 mol% Nd^{3+} ANPs at 77 K. Red data points represent simulating with increasing powers (up scan) and blue with decreasing (down scan). Switch-on (red) and switch-off (blue) power density thresholds are also shown. Legend: w/o KO – wild-type simulation, knock-outs (KOs): CR1 – $(^4I_{9/2} \rightarrow {}^4I_{11/2}):(^4I_{13/2} \rightarrow {}^4I_{11/2})$, CR2 – $(^4I_{9/2} \rightarrow {}^4I_{11/2}):(^4I_{15/2} \rightarrow {}^4I_{13/2})$, CR3 – $(^4I_{9/2} \rightarrow {}^4I_{15/2}):(^4F_{3/2} \rightarrow {}^4I_{15/2})$, CR4 – $(^4I_{9/2} \rightarrow {}^4I_{15/2}):(^4F_{3/2} \rightarrow {}^4I_{13/2})$, CR5 – $(^4I_{9/2} \rightarrow {}^4I_{13/2}):(^4F_{3/2} \rightarrow {}^4I_{15/2})$. The knocked-out cross-relaxation processes are shown in a simplified Nd^{3+} energy level diagram below.

11.2 Supplementary Note S2. Results of a simplified rate equation model

To summarize the photon avalanching mechanism by the most critical transitions in KPb_2Cl_5: 20 mol% Nd^{3+}, we simulated the power dependence of the system using only the first 7 energy states of Nd^{3+} ions (Supplementary Figure S12). The simulation accurately reproduced the experimental observations of luminescence hysteresis and population inversion and allowed to simplify the visualization of photo-activation mechanisms (Supplementary Figure S13).

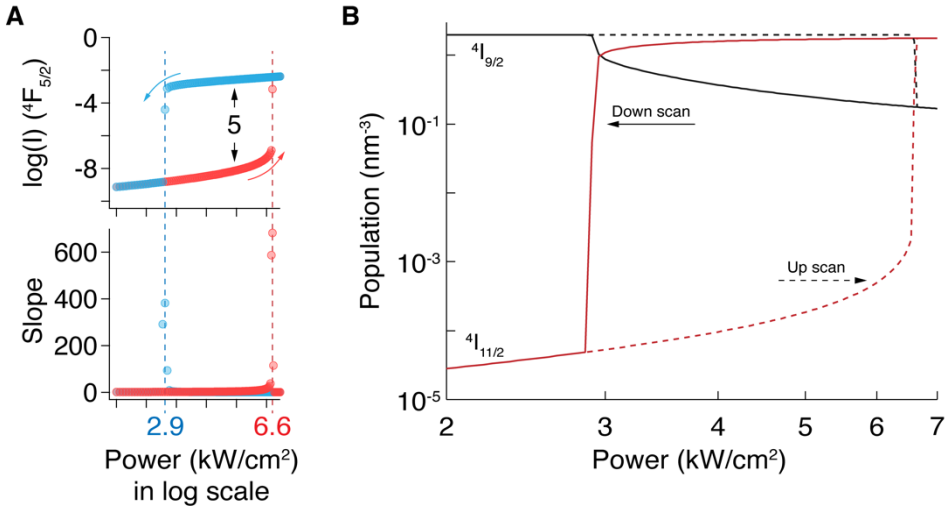

Supplementary Figure S12. A – Simulated pump (1064 nm) power dependence of Nd^{3+} emission (810 nm, $^4F_{5/2} \rightarrow {}^4I_{9/2}$) in KPb_2Cl_5: 20 mol% Nd^{3+} ANPs at 77 K, accounting only the first 7 energy levels (from $^4I_{9/2}$ to $^4F_{5/2}$) of Nd^{3+} ions. Red data points represent simulating increasing powers (up scan) and blue with decreasing (down scan). The switch-on (red) and switch-off (blue) power density thresholds are also shown. Arrows indicate a power density (black) within the bistable region for which the photo-activation mechanisms are shown in Supplementary Figure S13. **B** – Simulated pump (1064 nm) power dependence of Nd^{3+} ground ($^4I_{9/2}$) and first excited ($^4I_{11/2}$) states population in KPb_2Cl_5: 20 mol% Nd^{3+} ANPs at 77 K, accounting only the first 7 energy levels (from $^4I_{9/2}$ to $^4F_{5/2}$) of Nd^{3+} ions. Dashed lines indicate simulating with increasing powers (up scan) and solid with decreasing (down scan).

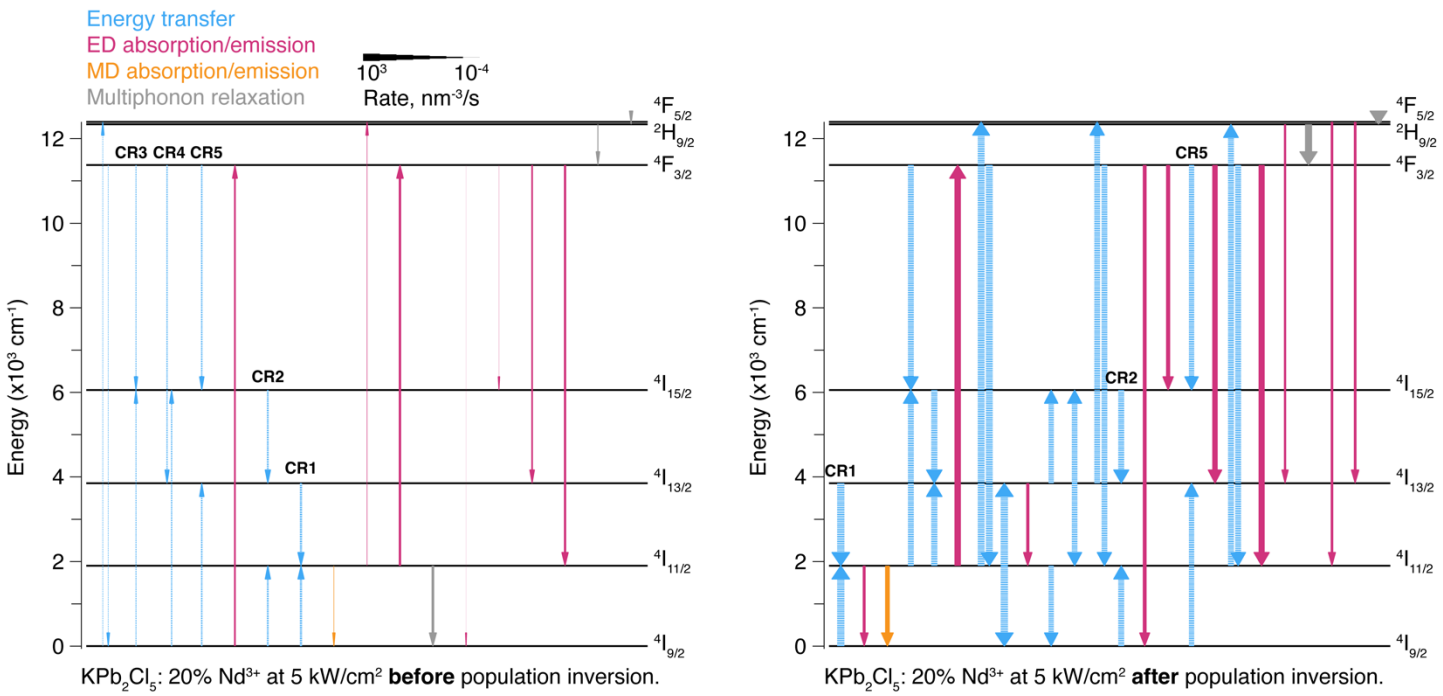

Supplementary Figure S13. Simplified energy level diagram and photophysical mechanism in KPb_2Cl_5: 20 mol% Nd^{3+} ANPs at 77 K, accounting only for the first 7 energy levels (from $^4I_{9/2}$ to $^4F_{5/2}$) of Nd^{3+} ions. The two diagrams represent primary energy transfer (blue arrows), photon absorption/emission (pink and yellow arrows), and multiphonon relaxation (gray arrows) processes in KPb_2Cl_5: 20 mol% Nd^{3+} ANPs at the same 1064 nm pump power density of 5 kW/cm^2 when in the dark (left panel, before switch-on) or bright states (right panel, after switch-on).

11.3 Additional data for mechanistic investigations

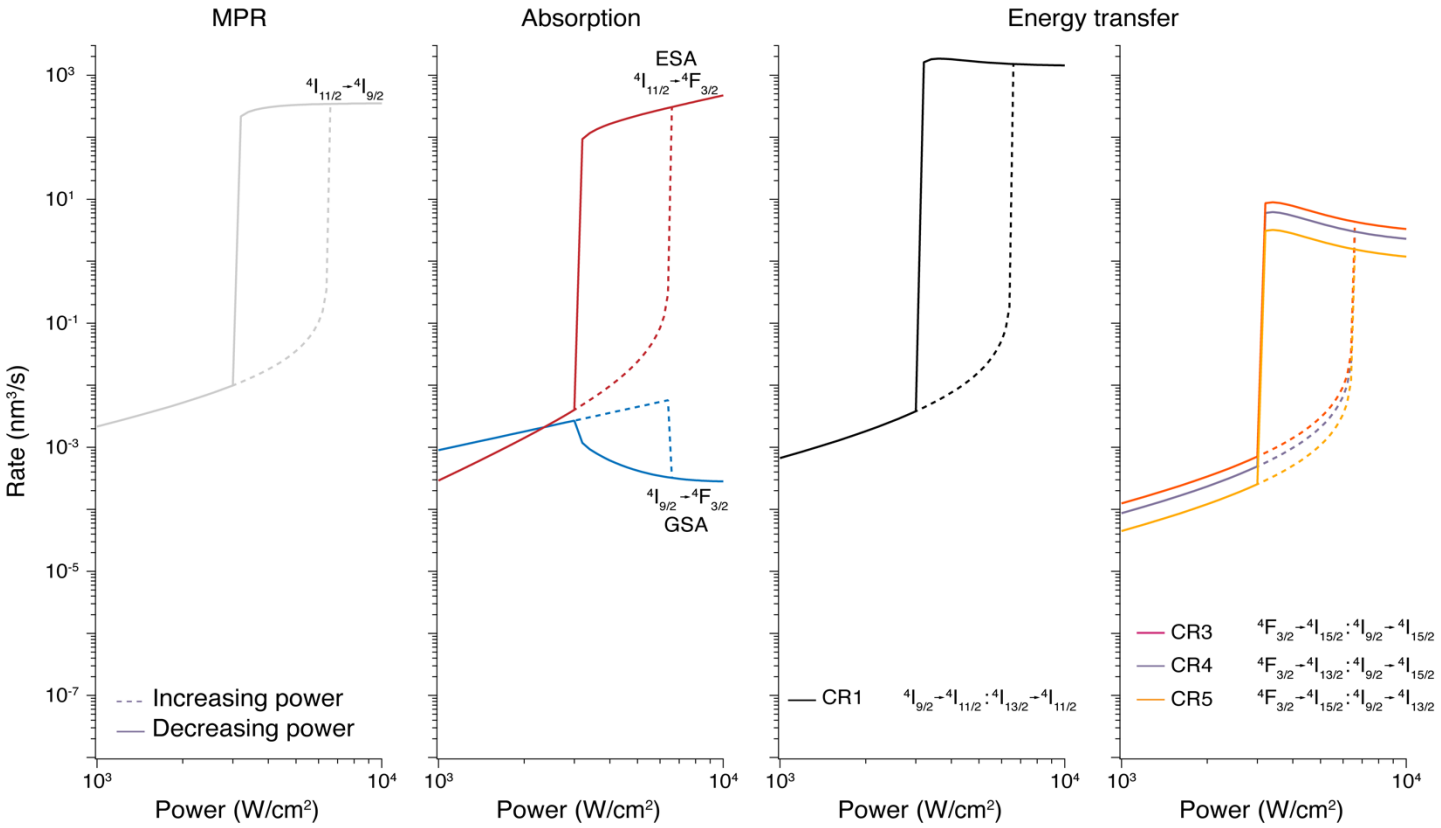

Supplementary Figure S14. Simulated pump (1064 nm) power dependence of different Nd^{3+} transitions in KPb_2Cl_5: 20 mol% Nd^{3+} ANPs. MPR – multiphoton relaxation, ESA – excited state absorption, GSA – ground state absorption, CR – cross-relaxation.

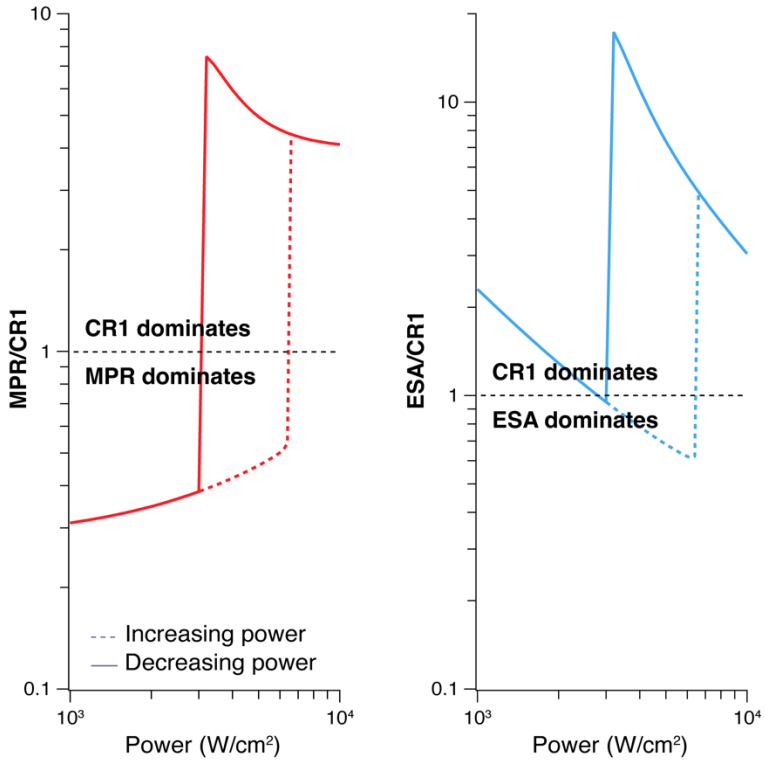

Supplementary Figure S15. Simulated pump (1064 nm) power-dependent ratio of MPR/CR1 (left) and ESA/CR1 (right) in KPb_2Cl_5: 20 mol% Nd^{3+} ANPs. When the bistable KPb_2Cl_5:Nd^{3+} ANPs are in their bright state, the CR1 dominates over MPR (left panel). Similarly, to sustain a positive feedback loop that leads to bistability, ESA and CR1 tradeoff in their contribution. Before the switch-on threshold, the probability of ESA increases with increasing pump power density and is the determining factor that switches the bistable ANPs from their dark to a bright state (right panel, dashed line). However, in the bright state, CR1 dominates over ESA, and with decreasing pump powers, compensates for the diminishing rate of ESA.

Pathway analysis. To determine the most critical transitions for a given energy transfer pathway, we considered only transitions with the highest branching fractions (β_{ij}) or contribution fractions (κ_{ij}), where:

$$\beta_{ij,t} = \frac{\left(\frac{dN_i}{dt}\right)^t_{i\to j}}{\sum_{t=ED,MD,ET,MPR}\sum_m \left(\frac{dN_i}{dt}\right)^t_{i\to m}} \tag{S21}$$

$$\kappa_{ij,t} = \frac{\left(\frac{dN_j}{dt}\right)^t_{i\to j}}{\sum_t \sum_m \left(\frac{dN_j}{dt}\right)^t_{m\to j}} \tag{S22}$$

For a given transition type t (ED/MD radiative, ET, MPR) from i to j, κ_{ij} (β_{ij}) represents that transition's fractional contribution to the overall population (depletion) of j (i) by all types of transitions to (from) level j (i). The rates dN_i/dt are determined by the populations of the originating states and the corresponding microscopic rate constants, as shown by the individual components of Equation S6. To select the most significant incoming transitions for each manifold i, we retained the transitions with the highest κ_{ij} that cumulatively contributed to over 90% of the respective population of j (i.e., $\sum \kappa_{ij}$ > 0.90). The most significant depopulating transitions can be filtered similarly using β_{ij} values.

The most important contributing and branching transitions in KPb_2Cl_5: 20 mol% Nd^{3+} before (dark state) and after (bright state) the switch-on power threshold are summarized in Supplementary Tables S6 and S7.

Supplementary Table S6. Major contributing transitions for KPb_2Cl_5: 20 mol% Nd^{3+} calculated at 5 kW/cm^2 at a steady state within the bistable region of luminescence before the switch-on threshold (power up) and after (power down). [a] Transitions in parentheses denote complementary ET transitions. [b] n/s – not significant.

			Power up		Power down	
Level i	Transition type	Transition $i \rightarrow j$[a]	Rate (nm^3/s)	κ_{ij}	Rate (nm^3/s)	κ_{ij}
$^4I_{9/2}$	MPR	$^4I_{11/2} \rightarrow {}^4I_{9/2}$	0.0357	0.9626	330.7373	0.1829
	ET acceptor	$^4I_{11/2} \rightarrow {}^4I_{9/2}$ ($^4I_{11/2} \rightarrow {}^4I_{13/2}$)	n/s[b]	n/s	1408.058	0.7788
$^4I_{11/2}$	ET acceptor	$^4I_{9/2} \rightarrow {}^4I_{11/2}$ ($^4I_{13/2} \rightarrow {}^4I_{11/2}$)	0.0164	0.2688	1638.3481	0.4181
	ET donor	$^4I_{13/2} \rightarrow {}^4I_{11/2}$ ($^4I_{9/2} \rightarrow {}^4I_{11/2}$)	0.0164	0.2688	1638.3481	0.4181
	ET donor	$^4F_{3/2} \rightarrow {}^4I_{11/2}$ ($^4I_{11/2} \rightarrow {}^4F_{5/2}$)	n/s	n/s	170.1308	0.0434
	ET acceptor	$^4I_{9/2} \rightarrow {}^4I_{11/2}$ ($^4I_{15/2} \rightarrow {}^4I_{13/2}$)	0.0068	0.1118	n/s	n/s
	ED em.	$^4F_{3/2} \rightarrow {}^4I_{11/2}$	0.0190	0.3109	43.0233	0.0110
$^4I_{13/2}$	ET acceptor	$^4I_{9/2} \rightarrow {}^4I_{13/2}$ ($^4F_{3/2} \rightarrow {}^4I_{15/2}$)	0.0030	0.1841	n/s	n/s
	ET donor	$^4I_{15/2} \rightarrow {}^4I_{13/2}$ ($^4I_{9/2} \rightarrow {}^4I_{11/2}$)	0.0068	0.4152	56.9246	0.0300
	ET acceptor	$^4I_{11/2} \rightarrow {}^4I_{13/2}$ ($^4I_{15/2} \rightarrow {}^4I_{13/2}$)	n/s	n/s	106.4997	0.0562
	ET donor	$^4I_{15/2} \rightarrow {}^4I_{13/2}$ ($^4I_{11/2} \rightarrow {}^4I_{13/2}$)	n/s	n/s	106.4997	0.0562
	ET acceptor	$^4I_{11/2} \rightarrow {}^4I_{13/2}$ ($^4I_{11/2} \rightarrow {}^4I_{9/2}$)	n/s	n/s	1408.0580	0.7424
	ED em.	$^4F_{3/2} \rightarrow {}^4I_{13/2}$	0.0036	0.2161	8.0558	0.0107
$^4I_{15/2}$	ET donor	$^4F_{3/2} \rightarrow {}^4I_{15/2}$ ($^4I_{9/2} \rightarrow {}^4I_{15/2}$)	0.0011	0.1447	n/s	n/s
	ET acceptor	$^4I_{9/2} \rightarrow {}^4I_{15/2}$ ($^4F_{3/2} \rightarrow {}^4I_{13/2}$)	0.0021	0.2802	n/s	n/s
	ET donor	$^4F_{3/2} \rightarrow {}^4I_{15/2}$ ($^4I_{9/2} \rightarrow {}^4I_{13/2}$)	0.0030	0.4034	5.8307	0.0337
	ET donor	$^4F_{3/2} \rightarrow {}^4I_{15/2}$ ($^4F_{3/2} \rightarrow {}^4G_{5/2}$)	n/s	n/s	13.5187	0.0781
	ET acceptor	$^4I_{13/2} \rightarrow {}^4I_{15/2}$ ($^4I_{11/2} \rightarrow {}^4I_{9/2}$)	n/s	n/s	21.4445	0.1239
	ET acceptor	$^4I_{11/2} \rightarrow {}^4I_{15/2}$ ($^4F_{3/2} \rightarrow {}^4I_{15/2}$)	n/s	n/s	23.8860	0.1380
	ET donor	$^4F_{3/2} \rightarrow {}^4I_{15/2}$ ($^4I_{11/2} \rightarrow {}^4I_{15/2}$)	n/s	n/s	23.8860	0.1380
	ET acceptor	$^4I_{13/2} \rightarrow {}^4I_{15/2}$ ($^4I_{13/2} \rightarrow {}^4I_{11/2}$)	n/s	n/s	46.6821	0.2698
	ED em.	$^4F_{3/2} \rightarrow {}^4I_{15/2}$	0.0002	0.0231	0.3935	0.0023
$^4F_{3/2}$	MPR	$^2H_{9/2} \rightarrow {}^4F_{3/2}$	0.0015	0.0464	511.3653	0.6775
	ED abs.	$^4I_{9/2} \rightarrow {}^4F_{3/2}$	0.0045	0.1428	n/s	n/s
	ED abs.	$^4I_{11/2} \rightarrow {}^4F_{3/2}$	0.0241	0.7653	222.8575	0.2952
$^2H_{9/2}$	MPR	$^4F_{5/2} \rightarrow {}^2H_{9/2}$	0.0012	0.8478	462.8812	0.9008
$^4F_{5/2}$	MPR	$^4F_{7/2} \rightarrow {}^4F_{5/2}$	0.0002	0.1623	220.2116	0.4722
	ET acceptor	$^4I_{9/2} \rightarrow {}^4F_{5/2}$ ($^4F_{3/2} \rightarrow {}^4I_{9/2}$)	0.0005	0.4296	n/s	n/s
	ET acceptor	$^4F_{3/2} \rightarrow {}^4F_{5/2}$ ($^4I_{13/2} \rightarrow {}^4I_{11/2}$)	n/s	n/s	17.5881	0.0377
	ET acceptor	$^4I_{11/2} \rightarrow {}^4F_{5/2}$ ($^4F_{3/2} \rightarrow {}^4I_{11/2}$)	n/s	n/s	170.1308	0.3648
	ED abs.	$^4I_{11/2} \rightarrow {}^4F_{5/2}$	0.0004	0.3553	n/s	n/s
$^4F_{7/2}$	MPR	$^4S_{3/2} \rightarrow {}^4F_{7/2}$	0.0002	0.7434	97.9593	0.4408
	ET donor	$^2H_{11/2} \rightarrow {}^4F_{7/2}$ ($^4I_{9/2} \rightarrow {}^4I_{11/2}$)	0.00002	0.1052	n/s	n/s
	ET donor	$^4F_{9/2} \rightarrow {}^4F_{7/2}$ ($^4I_{11/2} \rightarrow {}^4I_{13/2}$)	n/s	n/s	2.6266	0.0118
	ET acceptor	$^4F_{3/2} \rightarrow {}^4F_{7/2}$ ($^4I_{11/2} \rightarrow {}^4I_{9/2}$)	n/s	n/s	10.7590	0.0484
	ET acceptor	$^4F_{3/2} \rightarrow {}^4F_{7/2}$ ($^4I_{13/2} \rightarrow {}^4I_{11/2}$)	n/s	n/s	22.3553	0.1006
	ET acceptor	$^4I_{13/2} \rightarrow {}^4F_{7/2}$ ($^4F_{3/2} \rightarrow {}^4I_{11/2}$)	n/s	n/s	31.8461	0.1433
$^4S_{3/2}$	MPR	$^4F_{9/2} \rightarrow {}^4S_{3/2}$	0.0001	0.8966	59.1993	0.6017
	ET acceptor	$^4I_{13/2} \rightarrow {}^4S_{3/2}$ ($^4F_{3/2} \rightarrow {}^4I_{11/2}$)	n/s	n/s	23.6961	0.2408

Supplementary Table S7. Major branching transitions for KPb_2Cl_5: 20 mol% Nd^{3+} calculated at 5 kW/cm^2 at a steady state within the bistable region of luminescence before the switch-on threshold (power up) and after (power down). [a] Transitions in parentheses denote complementary ET transitions. [b] n/s – not significant.

			Power up		Power down	
Level i	Transition type	Transition $i \rightarrow j$[a]	Rate (nm^3/s)	β_{ij}	Rate (nm^3/s)	β_{ij}
$^4I_{9/2}$	ET acceptor	$^4I_{9/2} \rightarrow {}^4F_{5/2}$ ($^4F_{3/2} \rightarrow {}^4I_{9/2}$)	0.0005	0.0144	n/s[b]	n/s
	ET acceptor	$^4I_{9/2} \rightarrow {}^4I_{15/2}$ ($^4F_{3/2} \rightarrow {}^4I_{13/2}$)	0.0021	0.0567	n/s	n/s
	ET acceptor	$^4I_{9/2} \rightarrow {}^4I_{13/2}$ ($^4F_{3/2} \rightarrow {}^4I_{15/2}$)	0.0030	0.0816	n/s	n/s
	ET acceptor	$^4I_{9/2} \rightarrow {}^4I_{11/2}$ ($^4I_{15/2} \rightarrow {}^4I_{13/2}$)	0.0068	0.1840	n/s	n/s
	ET acceptor	$^4I_{9/2} \rightarrow {}^4I_{11/2}$ ($^4I_{13/2} \rightarrow {}^4I_{11/2}$)	0.0164	0.4423	1638.3481	0.9062
	ED abs.	$^4I_{9/2} \rightarrow {}^4F_{3/2}$	0.0045	0.1211	n/s	n/s
$^4I_{11/2}$	MPR	$^4I_{11/2} \rightarrow {}^4I_{9/2}$	0.0357	0.5852	330.7373	0.0844
	ET acceptor	$^4I_{11/2} \rightarrow {}^4F_{5/2}$ ($^4F_{3/2} \rightarrow {}^4I_{11/2}$)	n/s	n/s	170.1308	0.0434
	ET acceptor	$^4I_{11/2} \rightarrow {}^4I_{13/2}$ ($^4I_{11/2} \rightarrow {}^4I_{9/2}$)	n/s	n/s	1408.0580	0.3593
	ET donor	$^4I_{11/2} \rightarrow {}^4I_{9/2}$ ($^4I_{11/2} \rightarrow {}^4I_{13/2}$)	n/s	n/s	1408.0580	0.3593
	ED abs.	$^4I_{11/2} \rightarrow {}^4F_{3/2}$	0.0241	0.3943	222.8575	0.0569
$^4I_{13/2}$	ET acceptor	$^4I_{13/2} \rightarrow {}^4I_{15/2}$ ($^4I_{13/2} \rightarrow {}^4I_{11/2}$)	n/s	n/s	46.6821	0.0246
	ET donor	$^4I_{13/2} \rightarrow {}^4I_{11/2}$ ($^4I_{9/2} \rightarrow {}^4I_{11/2}$)	0.0164	0.9979	1638.3481	0.8638
	ET acceptor	$^4I_{13/2} \rightarrow {}^4F_{7/2}$ ($^4F_{3/2} \rightarrow {}^4I_{11/2}$)	n/s	n/s	31.8461	0.0168
$^4I_{15/2}$	ET donor	$^4I_{15/2} \rightarrow {}^4I_{13/2}$ ($^4I_{9/2} \rightarrow {}^4I_{11/2}$)	0.0068	0.9095	56.9246	0.3289
	ET donor	$^4I_{15/2} \rightarrow {}^4I_{13/2}$ ($^4I_{11/2} \rightarrow {}^4I_{13/2}$)	n/s	n/s	106.4997	0.6154
$^4F_{3/2}$	ET acceptor	$^4F_{3/2} \rightarrow {}^4G_{5/2}$ ($^4F_{3/2} \rightarrow {}^4I_{15/2}$)	n/s	n/s	13.5187	0.0179
	ET donor	$^4F_{3/2} \rightarrow {}^4I_{15/2}$ ($^4F_{3/2} \rightarrow {}^4G_{5/2}$)	n/s	n/s	13.5187	0.0179
	ET donor	$^4F_{3/2} \rightarrow {}^4I_{13/2}$ ($^4F_{3/2} \rightarrow {}^4G_{7/2}$)	n/s	n/s	39.3544	0.0521
	ET acceptor	$^4F_{3/2} \rightarrow {}^4G_{7/2}$ ($^4F_{3/2} \rightarrow {}^4I_{13/2}$)	n/s	n/s	39.3544	0.0521
	ET acceptor	$^4F_{3/2} \rightarrow {}^4F_{7/2}$ ($^4I_{11/2} \rightarrow {}^4I_{9/2}$)	n/s	n/s	10.7590	0.0143
	ET donor	$^4F_{3/2} \rightarrow {}^4I_{11/2}$ ($^4I_{13/2} \rightarrow {}^4S_{3/2}$)	n/s	n/s	23.6961	0.0314
	ET donor	$^4F_{3/2} \rightarrow {}^4I_{11/2}$ ($^4I_{13/2} \rightarrow {}^4F_{7/2}$)	n/s	n/s	31.8461	0.0422
	ET donor	$^4F_{3/2} \rightarrow {}^4I_{11/2}$ ($^4I_{11/2} \rightarrow {}^4F_{5/2}$)	n/s	n/s	170.1308	0.2254
	ET donor	$^4F_{3/2} \rightarrow {}^4I_{15/2}$ ($^4I_{9/2} \rightarrow {}^4I_{15/2}$)	0.0011	0.0345		
	ET donor	$^4F_{3/2} \rightarrow {}^4I_{15/2}$ ($^4I_{9/2} \rightarrow {}^4I_{13/2}$)	0.0030	0.0963	5.8307	0.0077
	ET acceptor	$^4F_{3/2} \rightarrow {}^4G_{9/2}$ ($^4F_{3/2} \rightarrow {}^4I_{13/2}$)	n/s	n/s	35.1088	0.0465
	ET donor	$^4F_{3/2} \rightarrow {}^4I_{13/2}$ ($^4F_{3/2} \rightarrow {}^4G_{9/2}$)	n/s	n/s	35.1088	0.0465
	ET acceptor	$^4F_{3/2} \rightarrow {}^4F_{5/2}$ ($^4I_{13/2} \rightarrow {}^4I_{11/2}$)	n/s	n/s	17.5881	0.0233
	ET donor	$^4F_{3/2} \rightarrow {}^4I_{11/2}$ ($^4I_{13/2} \rightarrow {}^4F_{5/2}$)	n/s	n/s	20.5211	0.0272
	ET acceptor	$^4F_{3/2} \rightarrow {}^4F_{7/2}$ ($^4I_{13/2} \rightarrow {}^4I_{11/2}$)	n/s	n/s	22.3553	0.0296
	ET donor	$^4F_{3/2} \rightarrow {}^4I_{15/2}$ ($^4I_{11/2} \rightarrow {}^4I_{15/2}$)	n/s	n/s	23.8860	0.0316
	ET donor	$^4F_{3/2} \rightarrow {}^4I_{11/2}$ ($^4I_{11/2} \rightarrow {}^2H_{9/2}$)	n/s	n/s	23.9986	0.0318
	ED em.	$^4F_{3/2} \rightarrow {}^4I_{9/2}$	0.0001	0.0038	0.2725	0.0004
	ED em.	$^4F_{3/2} \rightarrow {}^4I_{11/2}$	0.0190	0.6034	43.0233	0.0570
	ED em.	$^4F_{3/2} \rightarrow {}^4I_{13/2}$	0.0036	0.1130	8.0558	0.0107
	ED em.	$^4F_{3/2} \rightarrow {}^4I_{15/2}$	0.0002	0.0055	0.3935	0.0005
$^2H_{9/2}$	MPR	$^2H_{9/2} \rightarrow {}^4F_{3/2}$	0.0015	0.9991	511.3653	0.9952
$^4F_{5/2}$	MPR	$^4F_{5/2} \rightarrow {}^2H_{9/2}$	0.0012	0.9977	462.8812	0.9926
$^4F_{7/2}$	MPR	$^4F_{7/2} \rightarrow {}^4F_{5/2}$	0.0002	0.9969	220.2116	0.9909
$^4S_{3/2}$	MPR	$^4S_{3/2} \rightarrow {}^4F_{7/2}$	0.0002	0.9995	97.9593	0.9956
$^4F_{7/2}$	MPR	$^4F_{9/2} \rightarrow {}^4S_{3/2}$	0.0001	0.8404	59.1993	0.6776
	ET donor	$^4F_{9/2} \rightarrow {}^4F_{5/2}$ ($^4I_{11/2} \rightarrow {}^4I_{13/2}$)	n/s	n/s	3.5064	0.0401
	ET donor	$^4F_{9/2} \rightarrow {}^4I_{13/2}$ ($^4I_{11/2} \rightarrow {}^4F_{7/2}$)	n/s	n/s	2.3896	0.0274
	ET donor	$^4F_{9/2} \rightarrow {}^4I_{13/2}$ ($^4I_{11/2} \rightarrow {}^4F_{5/2}$)	n/s	n/s	2.5531	0.0292
	ET donor	$^4F_{9/2} \rightarrow {}^4F_{7/2}$ ($^4I_{11/2} \rightarrow {}^4I_{13/2}$)	n/s	n/s	2.6266	0.0301

12. Temporal modulation of IOB

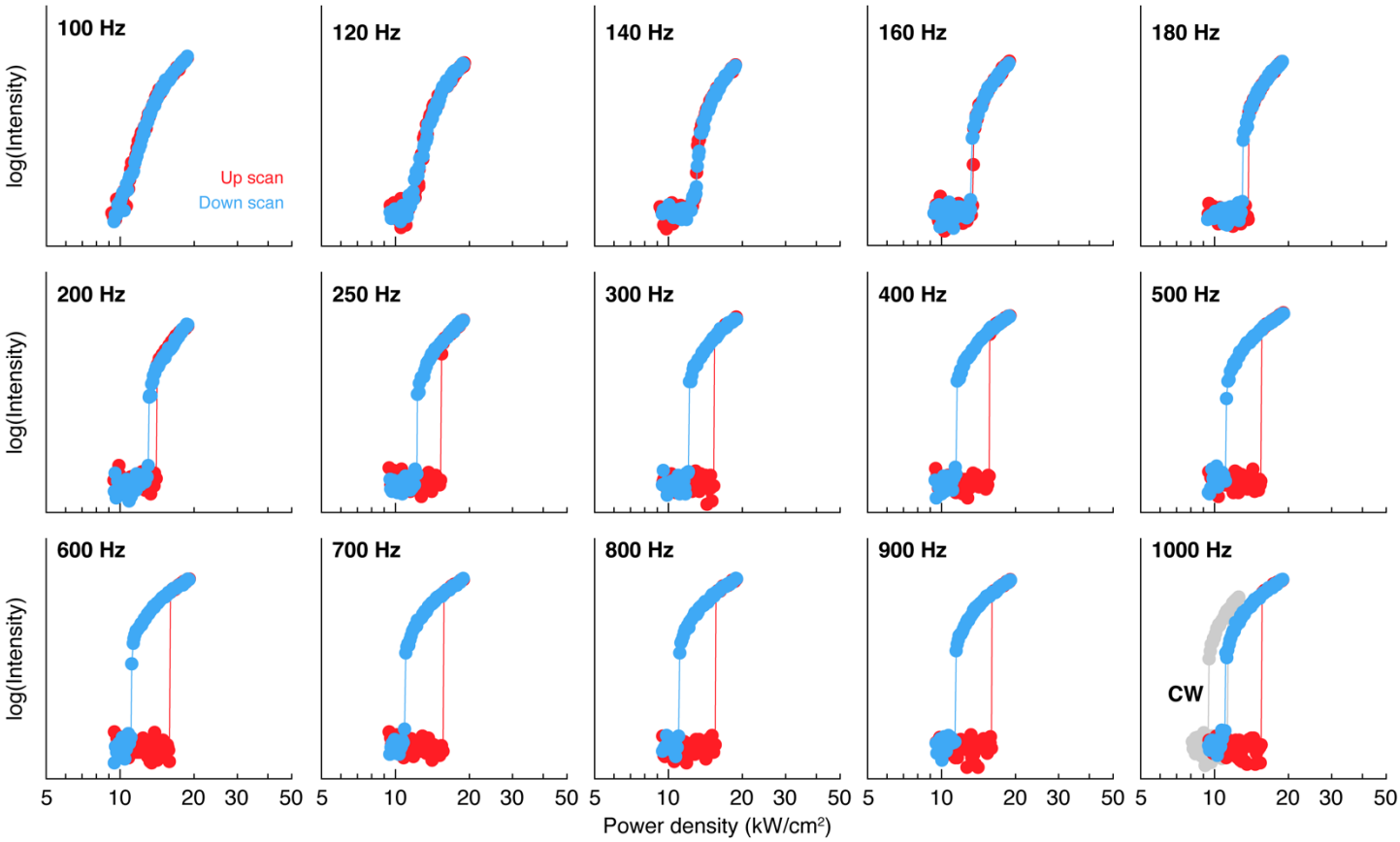

Supplementary Figure S16. Representative average pump (1064 nm) power dependence curves of Nd^{3+} emission (810 nm, $^4F_{5/2} \rightarrow {}^4I_{9/2}$) in $KPb_2Cl_5:Nd^{3+}$ ANPs at 77 K under pulsed pump of different frequencies (40% duty cycle). CW – continuous wave data are shown for comparison in a 1000 Hz panel. Red data points represent scanning with increasing powers (up scan) and blue with decreasing (down scan).

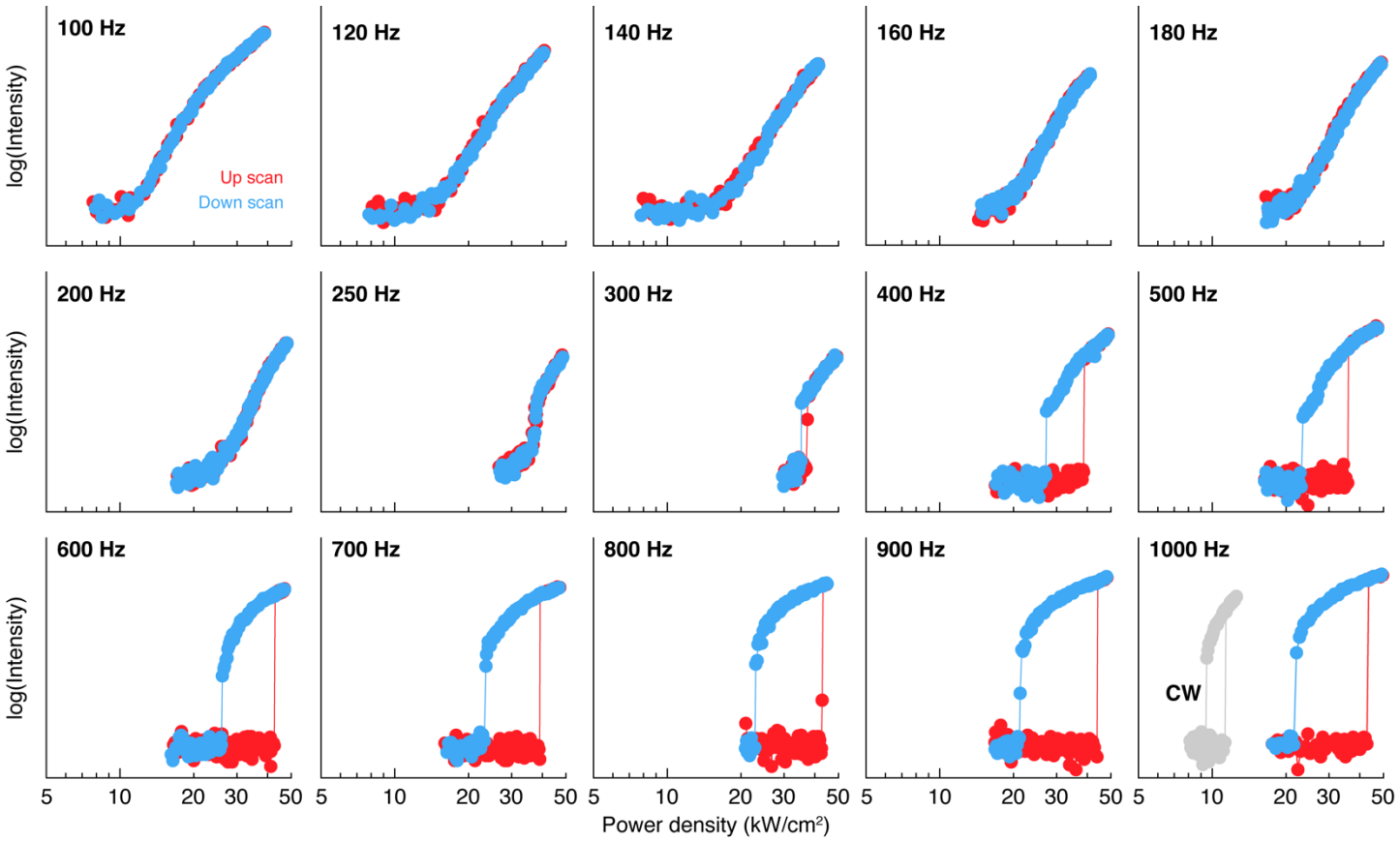

Supplementary Figure S17. Representative average pump (1064 nm) power dependence curves of Nd^{3+} emission (810 nm, $^4F_{5/2} \rightarrow {}^4I_{9/2}$) in $KPb_2Cl_5:Nd^{3+}$ ANPs at 77 K under pulsed pump of different frequencies (10% duty cycle). CW – continuous wave data are shown for comparison in a 1000 Hz panel. Red data points represent scanning with increasing powers (up scan) and blue with decreasing (down scan).

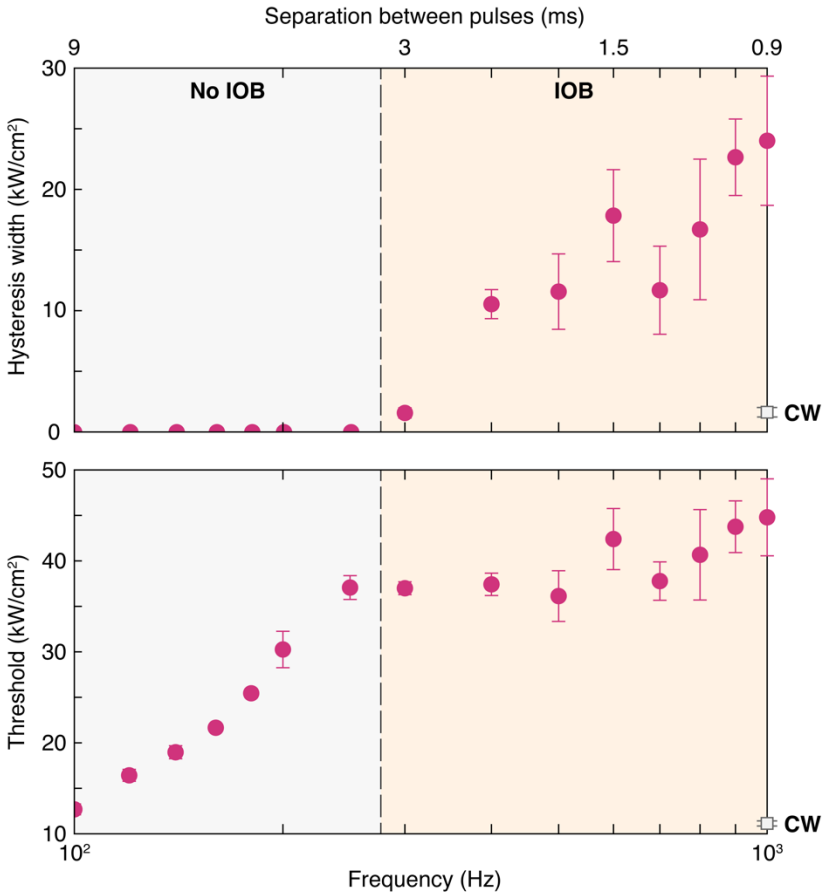

Supplementary Figure S18. Hysteresis width and photon avalanche switch-on threshold vs pump pulse frequency (10% duty cycle). Data is summarized from the Supplementary Figure S17. The corresponding time separation between pulses is also shown. Respective values under the CW pump are shown as squares. The data points are shown as the mean values ± 1 standard deviation (*n* = 3).

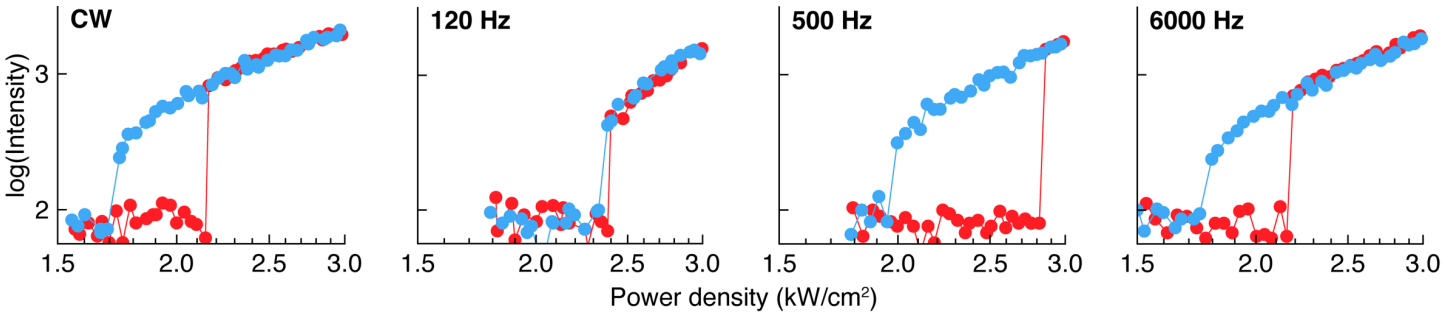

Supplementary Figure S19. Representative average pump (1064 nm) power dependence curves of Nd^{3+} emission (810 nm, $^4F_{5/2} \rightarrow {}^4I_{9/2}$) in $KPb_2Cl_5:Nd^{3+}$ ANPs at 77 K under continuous wave and the pulsed pump of different frequencies (50% duty cycle). Red data points represent scanning with increasing powers (up scan) and blue with decreasing (down scan).

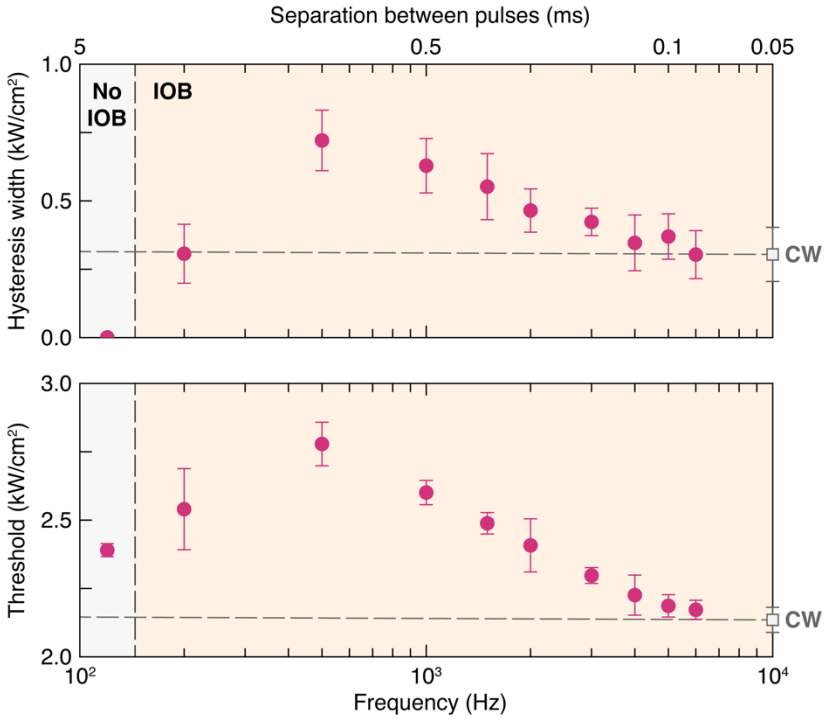

Supplementary Figure S20. Hysteresis width and photon avalanche switch ON threshold vs pump pulse frequency (50% duty cycle). Data is summarized from Figure S19. The corresponding time separation between pulses is also shown. At higher pump pulse frequencies, >4000 Hz, a quasi-CW regime is reached, and luminescence hysteresis of the $KPb_2Cl_5:Nd^{3+}$ ANPs matches that measured under the CW pump (shown as squares). The data points are shown as the mean values ± 1 standard deviation (n = 3).

Supplementary Note S3. Time-resolved measurements of ANPs

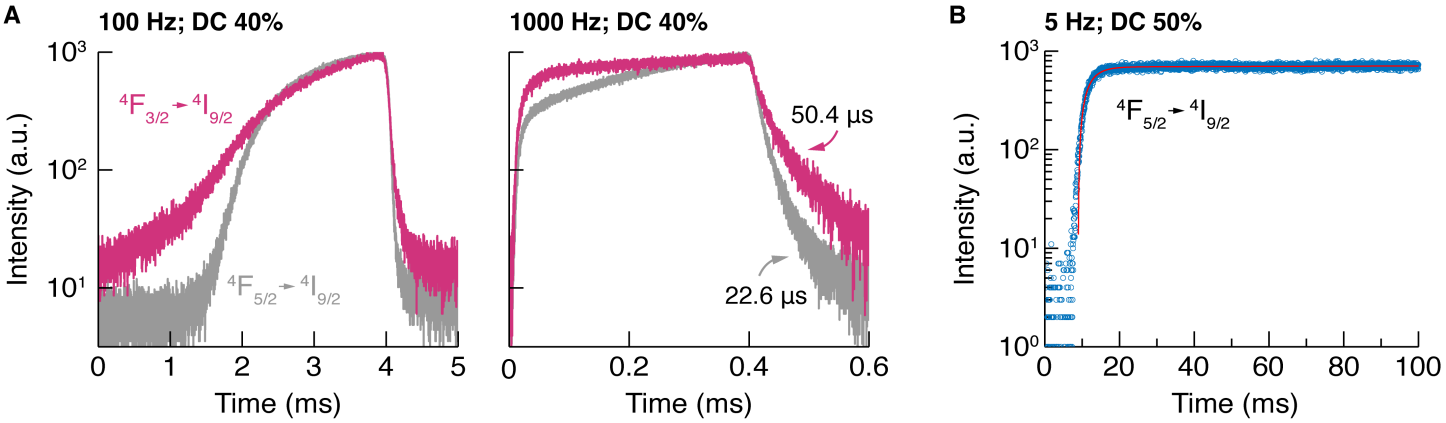

Supplementary Figure S21. Time-resolved photoluminescence of $KPb_2Cl_5:Nd^{3+}$ ANPs at 77 K measured for 880 nm ($^4F_{3/2} \rightarrow {}^4I_{9/2}$) and 810 nm ($^4F_{5/2} \rightarrow {}^4I_{9/2}$) optical transitions under the pulsed 1064 nm pump of different frequencies. The pulsed pump duty cycle was constant at 40%. The pulse frequencies of 100 Hz and 1000 Hz correspond to $KPb_2Cl_5:Nd^{3+}$ nanocrystals responding as regular or bistable ANPs, respectively (see Supplementary Figure S16 for power-dependent data). In the bistable excitation regime (1000 Hz), the rise time for populating $^4F_{3/2}$ energy level is 305 µs (calculated at 95% intensity from the steady state), and the decay times are 50.4 µs and 22.6 µs for $^4F_{3/2}$ and $^4F_{5/2}$ energy levels, respectively. The decay times were calculated by integrating the area under decay curves[31]. The estimated decay times are on the order of those measured for highly doped $NaGdF_4:Nd^{3+}$ and $LaPO_4:Nd^{3+}$ nanocrystals[41,42]. **B** - Time-resolved photoluminescence of $KPb_2Cl_5:Nd^{3+}$ ANPs at 77 K measured for 810 nm ($^4F_{5/2} \rightarrow {}^4I_{9/2}$) optical transition under a slow-pulsed 1064 nm pump (pulse frequency 5Hz, duty cycle 50%). Note, the measurement spot on the film sample is different than in **A**. The rise time for populating $^4F_{5/2}$ energy level is 20.8 ms (calculated at 95% intensity from the steady state). Blue circles are the experimental data points, and the red line is a double-exponential fit. Time-resolved photoluminescence was measured above the switch-on threshold at an average pump power intensity of 18.7 kW/cm^2 in **A** and 2.0 kW/cm^2 in **B**.

To better understand how pulsed modulation alters the luminescence hysteresis of $KPb_2Cl_5:Nd^{3+}$ ANPs, we performed time-resolved measurements for different pulsed excitation conditions (Supplementary Figure S21A). We note that with high-frequency pulsed excitation (e.g., 1000 Hz), emission of optically bistable ANPs is detected only in their bright state after the excitation threshold is reached (Supplementary Figure S16, 1000 Hz).

At high-frequency pulsed excitation, the population inversion (PI) of $^4I_{9/2}$ and $^4I_{11/2}$ energy levels persists between pulses, acting like a memory reservoir[43]. The time-resolved data (pink traces in Supplementary Figure S21) thus reflects the population of the $^4F_{3/2}$ emitting energy level directly via ESA, omitting the initial step of GSA. The observed delay in populating the $^4F_{5/2}$ energy level (gray traces in Supplementary Figure S21) results from the additional energy-transfer upconversion (Supplementary Figure S13).

In contrast, with low-frequency excitation pulses (e.g., 100 Hz) spaced further apart than the duration of PI, we observe a population of excited energy levels through a combination of GSA and ESA with each pulse. As a result, it takes several milliseconds for the ANPs to reach a quasi-steady state. To determine when these ANPs reach a steady state before saturation (i.e., bright state), we measured the population of $^4F_{5/2}$ excited energy level by modulating the 1064 nm pump at 5 Hz (Supplementary Figure S21B). Rise times of ca. 20 ms are measured in this case, shorter than for other ANPs or $KPb_2Cl_5:Nd^{3+}$ ANPs at RT[1].

Consequently, PA leading to the IOB is inherently faster than energy-looping processes reported in other ANPs. Optical bistable ANPs directly reach saturation at the threshold value when switched from a dark to a bright state without slow, intermediate photoluminescence.

13. Controlled photoswitching of the bistable $KPb_2Cl_5:Nd^{3+}$ nanocrystals

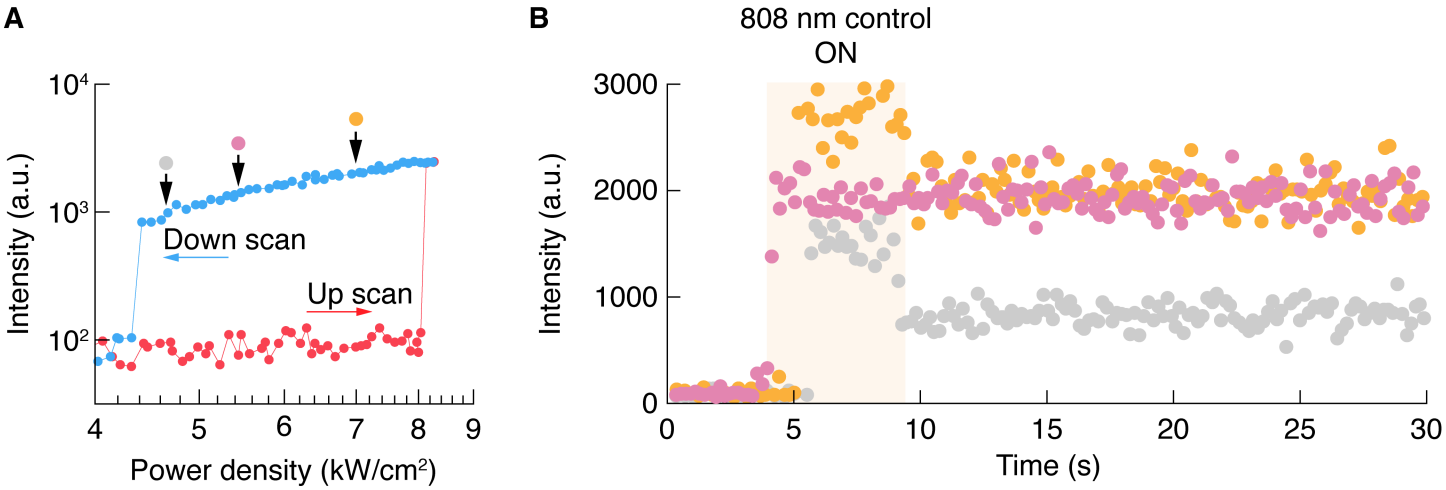

Supplementary Figure S22. A – Pump (**1064 nm, 40% duty cycle, 1000 Hz**) power dependence of the bistable $KPb_2Cl_5:Nd^{3+}$ nanocrystals used for photoswitching experiments with the indicated bias at different average power densities. **B** – Emission at 880 nm of the bistable $KPb_2Cl_5:Nd^{3+}$ nanocrystals before and after 808 nm control input. The increase in intensity when the 808 nm control input was switched ON is due to the control laser bleeding into the APD.

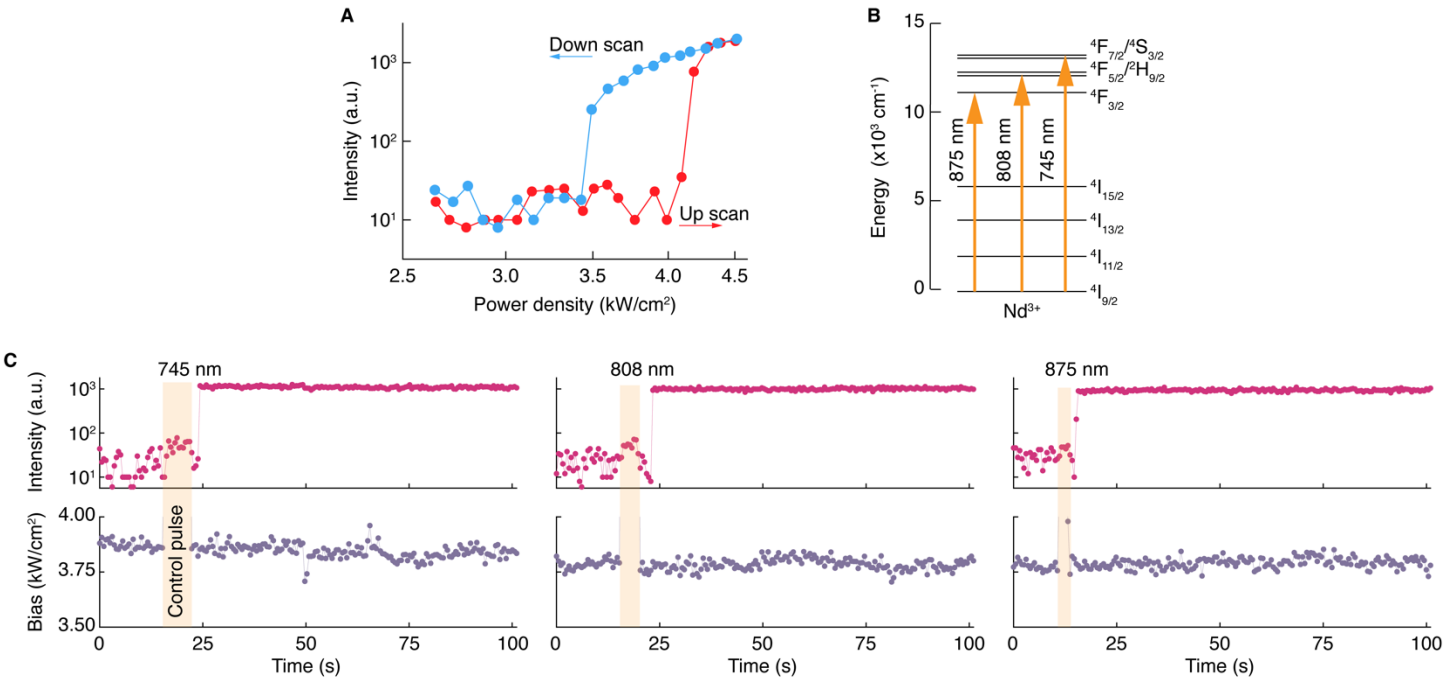

Supplementary Figure S23. **A** – Pump (1064 nm) power dependence of the bistable $KPb_2Cl_5:Nd^{3+}$ nanocrystals used for photoswitching experiments. **B** – A simplified Nd^{3+} energy level diagram with the indicated wavelengths of the control laser, matching ground state absorption of Nd^{3+} ions. **C** – time-dependent recording of 1064 nm bias power density and emission at 880 nm of the bistable $KPb_2Cl_5:Nd^{3+}$ nanocrystals before and after exposure to 745, 808, or 875 nm control pulse. Yellow shading indicates when the control input was switched ON and bled into the power meter. The delay in the emission detection is due to the shutter opening in the emission pathway after the control input ceases, which was used to avoid control laser bleeding into the APD.

14. Supplementary Discussion S1. Origins of IOB.

Our manuscript uses multiple lines of experimental and theoretical evidence to support our conclusion that IOB in $KPb_2Cl_5:Nd^{3+}$ nanocrystals is, in fact, non-thermal and distinct from the bistability of other Ln^{3+}-doped materials. While it is impossible to prove a mechanism, we rule out the most likely alternate hypotheses below.

This evidence includes:

1. Rate equation modeling reproduces the bistable photoluminescence of $KPb_2Cl_5:Nd^{3+}$ without any thermal inputs. To counter the hypothesis that our models include artifacts that lend themselves to IOB, we note that rate equation models developed independently from us have also been used to predict (but not experimentally realize) IOB in a Yb^{3+}, Tm^{3+} doped system without incorporating thermal effects[39].
2. If IOB were thermal in nature (e.g., beam-induced heating), one would expect that scanning through different excitation powers at different rates would alter the hysteresis and IOB, since the nanocrystals would experience more heating at longer dwell times. However, we show that this alternate thermal mechanism is unlikely because we still observe IOB of $KPb_2Cl_5:Nd^{3+}$ nanocrystals at different scan rates (Supplementary Figure S6), with little change in hysteresis width and with high reproducibility under continuous and pulsed laser irradiation (Supplementary Figure S16). One would also expect that heating would be dissipated under pulsed excitation at a low duty cycle, yet we still observe IOB in our system even when the laser is pulsed at a 10% duty cycle (Supplementary Figure S17).
3. If IOB were thermal in nature, requiring a full power sweep to trigger delayed avalanching, one would not expect to be able to photoswitch $KPb_2Cl_5:Nd^{3+}$ nanocrystals optically using a second, low-power laser (e.g. 808 nm), without going through a full power sweep. However, the transistor-like performance of $KPb_2Cl_5:Nd^{3+}$ nanocrystals shown in Fig. 5 and Supplementary Figures S22-23 demonstrates that we can indeed access all-optical photoswitching, allowing us to reject the thermal mechanism.
4. If the IOB were thermal in nature, one would expect that it would be highly dependent on the substrate since its thermal properties dictate the dissipation of heat. However, as we demonstrate in the Supplementary Figure S5, the IOB of $KPb_2Cl_5:Nd^{3+}$ nanocrystals does not depend on the substrate on which the nanocrystals were deposited, with luminescence hysteresis obtained on both glass and silicon substrates.
5. A thermal mechanism would require phonon emission to outcompete PA emission. However, multiphonon-relaxation rates are suppressed by the low-phonon-energy KPb_2Cl_5 host, while PA is highly efficient, especially at saturation where theoretical quantum yields can approach 40-50% (ref: 40).
6. As a final alternate mechanism, we consider that IOB might occur due to thermal nonlinearities driven by resonant ground state absorption (GSA) of the pump laser[12]. However, our PA nanocrystals are excited at a laser wavelength non-resonant with the GSA, reducing thermal loading and instead producing nonlinearity via electronic cross-relaxation processes. The non-resonant GSA is phonon-assisted, thus the efficient ESA+CR looping in PA effectively bypasses this GSA process. In fact, if thermal processes promoted GSA, this would be expected to decrease the nonlinearity of PA luminescence since PA

requires a high ratio (~10,000) of ESA rate to GSA rate. Since we still see extreme nonlinearities (200 and greater), we can dismiss this alternate mechanism.

Having ruled out the most likely alternate hypotheses and with rate equation modeling supporting the most simple explanation — an all-optical mechanism — we believe that the preponderance of the evidence, taken together, supports our assignment of a non-thermal IOB mechanism.

15. References

1. Zhang, Z. *et al.* Tuning Phonon Energies in Lanthanide-doped Potassium Lead Halide Nanocrystals for Enhanced Nonlinearity and Upconversion. *Angew. Chem. Int. Ed.* **62**, e202212549 (2023).
2. Ostrowski, A. D. *et al.* Controlled Synthesis and Single-Particle Imaging of Bright, Sub-10 nm Lanthanide-Doped Upconverting Nanocrystals. *ACS Nano* **6**, 2686–2692 (2012).
3. Cascales, C., Fernández, J. & Balda, R. Investigation of site-selective symmetries of Eu^{3+} ions in KPb_2Cl_5 by using optical spectroscopy. *Opt. Express* **13**, 2141 (2005).
4. Velázquez, M. *et al.* A Cationic Order-Disorder Phase Transition in KPb_2Cl_5. *Eur. J. Inorg. Chem.* **2006**, 4168–4178 (2006).
5. Marin, R. & Jaque, D. Doping Lanthanide Ions in Colloidal Semiconductor Nanocrystals for Brighter Photoluminescence. *Chem. Rev.* **121**, 1425–1462 (2021).
6. Nostrand, M. C., Page, R. H., Payne, S. A., Isaenko, L. I. & Yelisseyev, A. P. Optical properties of Dy^{3+} and Nd^{3+} doped KPb_2Cl_5. *J. Opt. Soc. Am. B* **18**, 264–276 (2021).
7. Nedelcu, G. *et al.* Fast Anion-Exchange in Highly Luminescent Nanocrystals of Cesium Lead Halide Perovskites ($CsPbX_3$, X = Cl, Br, I). *Nano Lett.* **15**, 5635–5640 (2015).
8. Huang, A., Duan, C.-K., Wong, K.-L. & Tanner, P. A. Downshifting in $Cs_2NaBiCl_6$:Er^{3+}: transforming ultraviolet into near infrared radiation. *J. Mater. Chem. C* **10**, 2950–2954 (2022).
9. Milstein, T. J. *et al.* Ubiquitous Near-Band-Edge Defect State in Rare-Earth-Doped Lead-Halide Perovskites. *Chem. Mater.* **34**, 3759–3769 (2022).
10. Kaminskii, A. A. *Crystalline Lasers: Physical Processes and Operating Schemes*. (CRC Press, 1996).
11. Suyver, J. F. *et al.* Upconversion spectroscopy and properties of $NaYF_4$ doped with Er^{3+}, Tm^{3+} and/or Yb^{3+}. *J. Lumin.* **117**, 1–12 (2006).
12. Gamelin, D. R., Lüthi, S. R. & Güdel, H. U. The Role of Laser Heating in the Intrinsic Optical Bistability of Yb^{3+} -Doped Bromide Lattices. *J. Phys. Chem. B* **104**, 11045–11057 (2000).
13. Neuendorf, R., Quinten, M. & Kreibig, U. Optical bistability of small heterogeneous clusters. *J. Chem. Phys.* **104**, 6348–6354 (1996).
14. Nishida, K. *et al.* Optical Bistability in Nanosilicon with Record Low *Q* -Factor. *Nano Lett.* **23**, 11727–11733 (2023).

15. Papas, D., Ou, J., Plum, E. & Zheludev, N. I. Microwatt Volatile Optical Bistability via Nanomechanical Nonlinearity. *Adv. Sci.* **10**, 2300042 (2023).

16. Ward, J. M., O'Shea, D. G., Shortt, B. J. & Chormaic, S. N. Optical bistability in Er-Yb codoped phosphate glass microspheres at room temperature. *J. Appl. Phys.* **102**, 023104 (2007).

17. Nozaki, K. *et al.* Ultralow-power all-optical RAM based on nanocavities. *Nat. Photon.* **6**, 248–252 (2012).

18. Li, L. *et al.* Bistable upconversion emission in Yb-sensitized Tm:ZrO_2 nanophosphors at room temperature. *J. Nonlinear Optic. Phys. Mat.* **25**, 1650009 (2016).

19. Marciniak, L., Strek, W., Bednarkiewicz, A., Lukowiak, A. & Hreniak, D. Bright upconversion emission of Nd^{3+} in $LiLa_{1-x}Nd_xP_4O_{12}$ nanocrystalline powders. *Opt. Mater.* **33**, 1492–1494 (2011).

20. Lüthi, S. R., Hehlen, M. P., Riedener, T. & Güdel, H. U. Excited-state dynamics and optical bistability in the dimer system $Cs_3Lu_2Br_9$: Yb^{3+}. *J. Lumin.* **76–77**, 447–450 (1998).

21. Ródenas, A. *et al.* Bistable chromatic switching in Yb^{3+}-doped $NdPO_4$ crystals. *Phys. Rev. B* **74**, 035106 (2006).

22. Redmond, S. M. & Rand, S. C. Intrinsic chromatic switching of visible luminescence in Yb^{3+},Er^{3+}+:$CsCdBr_3$. *Opt. Lett.* **28**, 173 (2003).

23. Hehlen, M. P., Kuditcher, A., Rand, S. C. & Lüthi, S. R. Site-Selective, Intrinsically Bistable Luminescence of Yb^{3+} Ion Pairs in $CsCdBr_3$. *Phys. Rev. Lett.* **82**, 3050–3053 (1999).

24. Li, D., Cui, H., Qin, G. & Qin, W. Photoinduced photon avalanche turns white objects into bright blackbodies. *Commun. Phys.* **6**, 120 (2023).

25. Kuditcher, A., Hehlen, M. P., Florea, C. M., Winick, K. W. & Rand, S. C. Intrinsic Bistability of Luminescence and Stimulated Emission in Yb- and Tm-Doped Glass. *Phys. Rev. Lett.* **84**, 1898–1901 (2000).

26. Soni, A. K. & Rai, V. K. Intrinsic optical bistability and frequency upconversion in Tm^{3+}-Yb^{3+}-codoped Y_2WO_6 phosphor. *Dalton Trans.* **43**, 13563–13570 (2014).

27. Ge, Q. *et al.* Optical bistability via an external control laser in an erbium-doped-fiber laser. *Opt. Laser Technol.* **98**, 79–83 (2018).

28. Zhang, Q. *et al.* Abnormal upconversion luminescence from Yb^{3+} doped and Tb^{3+}/Yb^{3+} codoped high silica glasses induced by intrinsic optical bistability. *Appl. Phys. B* **98**, 261–265 (2010).

29. Seaton, C. T., Smith, S. D., Tooley, F. A. P., Prise, M. E. & Taghizadeh, M. R. Realization of an InSb bistable device as an optical AND gate and its use to measure carrier recombination times. *Appl. Phys. Lett.* **42**, 131–133 (1983).

30. Chan, E. M., Gargas, D. J., Schuck, P. J. & Milliron, D. J. Concentrating and Recycling Energy in Lanthanide Codopants for Efficient and Spectrally Pure Emission: The Case of $NaYF_4$:Er^{3+}/Tm^{3+} Upconverting Nanocrystals. *J. Phys. Chem. B* **116**, 10561–10570 (2012).

31. Teitelboim, A. *et al.* Energy Transfer Networks within Upconverting Nanoparticles Are Complex Systems with Collective, Robust, and History-Dependent Dynamics. *J. Phys. Chem. C* **123**, 2678–2689 (2019).

32. Chan, E. M. Combinatorial approaches for developing upconverting nanomaterials: high-throughput screening, modeling, and applications. *Chem. Soc. Rev.* **44**, 1653–1679 (2015).

33. van Dijk, J. M. F. & Schuurmans, M. F. H. On the nonradiative and radiative decay rates and a modified exponential energy gap law for 4 *f* –4 *f* transitions in rare-earth ions. *J. Chem. Phys.* **78**, 5317–5323 (1983).

34. Walsh, B. M. Judd-Ofelt theory: principles and practices. in *Advances in Spectroscopy for Lasers and Sensing* (eds. Di Bartolo, B. & Forte, O.) 403–433 (Springer Netherlands, Dordrecht, 2006). doi:10.1007/1-4020-4789-4_21.

35. Isaenko, L. *et al.* New laser crystals based on KPb_2Cl_5 for IR region. *Mater. Sci. Eng. B* **81**, 188–190 (2001).

36. Kushida, T. Energy Transfer and Cooperative Optical Transitions in Rare-Earth Doped Inorganic Materials. I. Transition Probability Calculation. *J. Phys. Soc. Jpn.* **34**, 1318–1326 (1973).

37. Miyakawa, T. & Dexter, D. L. Phonon Sidebands, Multiphonon Relaxation of Excited States, and Phonon-Assisted Energy Transfer between Ions in Solids. *Phys. Rev. B* **1**, 2961–2969 (1970).

38. Auzel, F. & Pellé, F. Bottleneck in multiphonon nonradiative transitions. *Phys. Rev. B* **55**, 11006–11009 (1997).

39. Li, L., Zhang, X., Cui, J. & Chen, L. A theoretical study of intrinsic optical bistability dynamics in Tm^{3+}/Yb^{3+} codoped systems with an upconversion avalanche mechanism. *J. Opt. A: Pure Appl. Opt.* **11**, 105203 (2009).

40. Lee, C. *et al.* Giant nonlinear optical responses from photon-avalanching nanoparticles. *Nature* **589**, 230–235 (2021).

41. Skripka, A. *et al.* Inert Shell Effect on the Quantum Yield of Neodymium-Doped Near-Infrared Nanoparticles: The Necessary Shield in an Aqueous Dispersion. *Nano Lett.* **20**, 7648–7654 (2020).

42. Suta, M. *et al.* Making Nd^{3+} a Sensitive Luminescent Thermometer for Physiological Temperatures—An Account of Pitfalls in Boltzmann Thermometry. *Nanomaterials* **10**, 543 (2020).

43. Bednarkiewicz, A. *et al.* All-Optical Data Processing with Photon Avalanching Nanocrystalline Photonic Synapse. *Adv. Mater.* **35**, 2304390 (2023).